Hydrogeology Journal
https://doi.org/10.1007/s10040-025-02970-8

PAPER

Challenges in comparing land subsidence measurements by PS-InSAR with simulations from coupled hydro-geomechanical modelling: a case study in Antwerp Harbour

A. Choopani[1,2,3] · P. Orban[2] · P. Y. Declercq[1] · X. Devleeschouwer[1] · A. Dassargues[2]

Received: 6 July 2024 / Accepted: 15 October 2025

Abstract
Land subsidence is a serious problem in rapidly urbanizing areas like Antwerp, Belgium, where one known driver is the consolidation of Holocene sediments beneath the harbour's backfill. However, the potential contribution of groundwater abstraction to subsidence remains poorly understood, as deformation measurements from interferometric synthetic aperture radar (InSAR) alone cannot pinpoint subsurface processes. This study addresses this gap by investigating whether groundwater-induced consolidation also plays a role in subsidence in Antwerp Harbour. In this work, deformation estimates derived from persistent scatterer InSAR (PS-InSAR) and a 3D-MODFLOW groundwater flow model, sequentially coupled to a 1D-geomechanical model implemented in Python. The model captures delayed consolidation in low-permeability units. For modelling, a region outside the harbour's backfill was selected to exclude the influence of harbour sediment consolidation and isolate the potential role of groundwater abstraction, comparing observed and simulated deformations. Results show groundwater-induced consolidation contributes to subsidence rates of 1.78 mm/year (2009–2016), closely matching PS-InSAR estimates of –2.67, –2.39 and –2.43 mm/year from SkyGeo (2017–2022), EGMS (2019–2023), and TerraSAR-X (2019–2022), respectively. Validation of the PS-InSAR datasets was performed using GNSS station BEZA, with the EGMS showing the best fit. Results reveal groundwater level changes contribute to subsidence beyond natural sediment consolidation, although challenges such as data scarcity complicate direct comparisons. The insights point to groundwater as a likely additional factor in regional subsidence and emphasize the importance of improved data integration for refining hydro-geomechanical models to enhance subsidence predictions.

Keywords Subsidence · Aquitard compaction and swelling · Numerical modeling · Persistent scatterer interferometry · Geomechanical modelling

Introduction

Interferometric synthetic aperture radar (InSAR) measurements have provided new insights into land movement detection. Land subsidence or uplift, because of pore pressure changes induced by pumping or drainage, has been effectively monitored using this technique. InSAR effectively allows estimating land surface deformations over time. The displacement time series and land surface velocity map in the satellite line of sight (LOS) direction are the two primary outputs.

InSAR generates an interferogram using a pair of complex SAR images acquired at two distinct times and from slightly differing orbital positions. By analyzing the phase difference between these two acquisitions, the displacement of the ground surface can be determined along the satellite LOS (Massonnet and Feigl 1998; Chen et al. 2020). Global positioning system (GPS) campaigns, subsoil elevation surveys using cable or pipe borehole extensometers, and leveling, are traditional land subsidence assessment techniques that can provide data with millimeter-scale precision. However, these methods have several limitations. While

✉ A. Choopani
Atefe.choopani@doct.uliege.be; atefe.choopani@kuleuven.be

1 Institute of Natural Sciences, Geological Survey of Belgium, Brussels, Belgium

2 Hydrogeology and Environmental Geology, Urban and Environmental Engineering, University of Liège, Liege, Belgium

3 Present Address: Division of Forest, Nature and Landscape, KU Leuven, 3001 Leuven, Belgium

Published online: 13 November 2025

some can provide continuous data, they often do not offer continuous spatial coverage. They can be costly and time-consuming, especially when monitoring large areas. While they are invaluable for specific applications (e.g., borehole extensometers allow for the detection of consolidation in each layer), they might not always be the most practical choice for broad-scale and continuous monitoring (Zhou et al. 2019; Li et al. 2022a, b).

Multi-temporal InSAR (MT-InSAR) technology, because of its extensive geographical coverage and higher precision, can detect displacements with millimeter-level precision in the vertical direction (Ghorbani et al. 2022); under favourable conditions, the horizontal resolution approaches the metre scale. (Peng et al. 2022). This higher precision in the vertical direction makes MT-InSAR particularly valuable for monitoring small ground movements over time, compensating for the typical centimeter-level precision in conventional InSAR by using multiple temporal acquisitions to enhance measurement accuracy. This is one of the most cost-effective methods for assessing ground surface displacement over large areas. Resulting from the link between water pressure in hydrogeological layers and consolidation processes, InSAR has recently been employed as a basic dataset for the estimation of aquifer storage characteristics through inverse groundwater modelling (Chaussard et al. 2014; Miller and Shirzaei 2015; Miller et al. 2017; Motagh et al. 2017; Jiang et al. 2018; Gualandi and Liu 2021). Multi-temporal InSAR methods, including PS-InSAR (Ferretti et al. 2000, 2001) and the small baseline subset (SBAS) technique (Berardino et al. 2002), are among the predominant categories of InSAR techniques. They are primarily employed to mitigate the effects of atmospheric distortions and topographic inaccuracies, creating artifacts (Chen et al. 2021). Compared to PS-InSAR, the SBAS approach is more suitable for detecting displacement in areas with less stable or coherent reflectors, such as rural environments. However, the accuracy is primarily influenced by the characteristics of the Earth's surface, which can compromise vegetated regions with high temporal decorrelation (Xu et al. 2021). In highly vegetated regions or areas with significant surface changes, the temporal decorrelation can lead to challenges in phase unwrapping. Conversely, PS-InSAR identifies pixels exhibiting consistent and permanent scattering behaviour over time. This enables the mapping of displacement patterns and quantifies surface motion over extended periods, thereby addressing the limitations of the conventional InSAR approach (Ferretti et al. 2000, 2001, 2007; Fiorentini et al. 2020). However, while MT-InSAR methods provide a reliable integrated estimation of consolidation occurring below the surface, they do not provide information about the specific layers affected by the consolidation processes. Nevertheless, their contribution to understanding ground movement remains invaluable, and they have revealed cases that were previously undetected by other surveying techniques (Gambolati and Teatini 2015). However, despite its value in detecting surface deformation, InSAR alone cannot identify which subsurface layers are responsible for the observed movements.

To address these limitations, coupled hydrogeological and geomechanical models have been employed to simulate subsurface processes that contribute to land subsidence. While the methods employed in this study build on well-established principles of hydrogeological modelling and geomechanical behaviour, various methodologies have been developed over the years to address land subsidence caused by hydraulic head changes.

Initially, occurrences were primarily attributed to natural causes such as tectonic activities, karstification, and the natural compaction of sedimentary basins (Heiken et al. 2013). By the late 19th and early 20th centuries, human activities such as mining, gas or oil exploitation, and groundwater pumping, introduced a new set of challenges (Reddish and Whittaker 2012). Coal extraction, for instance, created voids that led to ground collapses (Forster 2000). In the 20th century, groundwater extraction became one of the primary causes of land subsidence. Extensive extraction from aquifers often resulted in a reduction of pore pressure, leading to the compaction of granular layers and subsidence at the surface (Poland and Davis 1969). Some of the most notable cases of subsidence from groundwater extraction include (among many others) the San Joaquin Valley in California and Mexico City (Galloway et al. 1999; Galloway and Riley 1999; Strozzi and Wegmuller 1999); Bangkok (Phien-wej et al. 2006); Venice (Gambolati et al. 1974; Tosi et al. 2009; Zanchettin et al. 2021); Tokyo (Sato et al. 2006); Shanghai (Dassargues et al. 1993a, b; Dong et al. 2014); Jakarta (Abidin et al. 2011); and Tehran (Tavakkoli Estahbanati and Dehghani 2018). The oil and gas industry is also confronted with significant subsidence induced by reservoir and overburden layers compaction and subsequent surface subsidence (Geertsma 1973; Ferretti 2014; van Thienen-Visser and Pruiksma 2015).

Initial efforts to model subsidence were largely empirical, particularly for groundwater-induced subsidence (Holzer and Bluntzer 1984). These models often drew correlations between water abstraction volumes and observed land subsidence. Statistical, semiempirical methods, including regression analysis (Allen 1973; Duncan and Chang 1970; Poulos et al. 2002) and 'black box' models (Phoon and Tang) were developed. However, they offer lower reliability, especially if they are used for prediction with stresses that are out of the calibration range (Wang et al. 2019). These models were constrained by encompassed assumptions of spatial-temporal uniformity, linear behaviour, a lack of mechanistic understanding, and a narrow focus on single variables, although a few did touch upon nonlinear behaviour with clear limitations (Burbey 2002; Domenico and Schwartz 1997; Galloway and Burbey 2011; Wang et al. 2019).

Subsequently, models began to incorporate theoretical and mechanistic elements, integrating soil mechanics and hydrogeology (Helm 1976; Gabrysch and Bonnet 1975; Holzer and Galloway 2005; Motagh et al. 2007). Building on a process-based approach, Terzaghi (1925) introduced a one-dimensional (1D) consolidation theory (Jaeger et al. 2009). This conceptual model linking the effective stress to the water pore pressure in saturated, compressible media allows for the coupling of equations of groundwater flow and geomechanical behaviour to predict time-dependent compaction of clays (Terzaghi 1943; Hubbert 1957; Poland and Davis 1969). Biot (1941) introduced a more encompassing poroelastic theory in 1941, which considered the interaction between soil matrix deformation and pore fluid movement in multiple dimensions; however, its extensive resource and data requirements limit its widespread application (Gambolati and Freeze 1973; Sukirman and Lewis 1994). This first generation of mathematical equations offered a deeper understanding of the intricate deformation processes, fluid migration, and the distribution of stress within underground formations (Detournay and Cheng 1993). Over time, the importance of modelling irreversible plastic behaviour became evident, leading to the incorporation of elasto-plastic formulations, including compressibility coefficients that depend on the stress state and stress history (Wood 1990). From this framework, the Cam-clay model emerged as a significant elastoplastic model for clays, providing insights into both consolidation and yield mechanisms (Schofield and Wroth 1968). More intricate models such as the modified Cam-clay for over-consolidated clays and the Hardening soil model for modelling stress-dependent stiffness and plastic behaviour in soils were developed (Roscoe and Burland 1968; Schanz 1998; Schanz et al. 1999). Viscoelastic models also emerged, blending theory and empirical observations to merge both elastic and viscous behaviours (Findley et al. 2013). Creep models capture time-dependent deformations experienced by saturated soils under constant effective stress loading (Yasuhara et al. 1986; Mitchell and Soga 2005), which can simulate substantial subsidence (Seed 1965).

In 1D flow and consolidation modelling, lateral strains and drainage are typically disregarded, implying that the movement of fluid and associated deformations are assumed to occur predominantly in the vertical direction (Davis and Raymond 1965; Schiffman and Stein 1970; Yun 2002; Radhika et al. 2020). In coupled three-dimensional (3D) flow and 1D consolidation models, groundwater movement is computed in 3D, while compaction is calculated exclusively in the vertical direction (Gambolati and Freeze 1973; Shen and Xu 2011; Xu et al. 2008).

Given the complexity of the land subsidence processes, the shortcomings of analytical solutions are evident (Lewis and Schrefler 1987). Numerical methods, based on finite difference methods (FDM) and finite element methods (FEM) (Zienkiewicz and Taylor 1989), are used. Other techniques like the boundary element method (BEM) (Mirsalari et al. 2017), mesh-free or meshless methods (Khoshghalb and Khalili 2010), Lattice Boltzmann method (LBM) (Kim et al. 2019), and discontinuous Galerkin methods (Chen et al. 2013) can also address the complex geomechanical issues (Galloway and Burbey 2011).

Land subsidence prediction is chiefly based on two coupled models that simultaneously examine groundwater flow and consolidation (Gambolati and Freeze 1973), requiring the development of advanced simulation software (Reddish and Whittaker 2012; Guzy and Malinowska 2020). COMPAC used an FDM method for pioneering the modelling of 1D consolidation in compacting aquifer systems (Helm 1986) considering vertical stresses in aquitards. This software was the first to allow simulation of recoverable and nonrecoverable consolidations (Helm 1976). The IBS1 tool, combined with MODFLOW for 3D regional groundwater flow, simulated subsidence in 'interbeds' layers (Prudic 1989), which are the compressible layers between high permeable aquifers. Despite the unrealistic assumption of an instant hydraulic head propagation in the compressible and low-permeability layers, hydrogeologists have used IBS1 extensively (Mahmoudpour et al. 2016). The SUB Package proposed with MODFLOW enabled the stimulation of time-dependent decrease in pressure propagation and compaction in thick, low-permeability units (Hoffmann et al. 2003). Earlier codes also used an approach with a single equivalent layer rather than distinct ones, preventing the garnering of individual subsidence results for each layer (Jafari et al. 2016; Choopani et al. 2019). The SUB-WT package for MODFLOW offers the possibility of a total stress variation (Leake and Galloway 2007; Leake and Galloway 2010). Beyond these mentioned codes, specific advanced modelling solutions were also developed by different research teams (Brinkgreve and Vermeer 1999; Calderhead et al. 2011; Hu et al. 2013; Pham et al. 2019; 2020)—for example, among the first ones, Dassargues et al. (1993a, b) developed a 3D FEM model for simulating transient groundwater pressure conditions in the area of Shanghai. This model was coupled to 30 vertical 1D flow-compaction geomechanical FEM models where pore pressure conditions on the boundaries of the aquifer layers were actualized at each time step from the 3D model. Specifically, this approach allowed for having a very fine discretization of the clay layers, which also allowed taking the hydraulic conductivity and specific storage variations (as a function of the stress-state) into account (Dassargues 1995). Also, compressibility is dependent on the reached effective stress influenced by the induced groundwater drawdown (Dassargues 1998; Guzy and Malinowska 2020).

More recently, the implementation of artificial intelligence (AI) and machine learning (ML) in geomechanical modelling is evolving, bringing improved simulation

efficiency and predictive capabilities (Baghbani et al. 2022; Zhang et al. 2023). In subsidence prediction and mapping, various AI methodologies have been adopted, including artificial neural networks (ANN) (Zhao and Chen 2011; Yang and Xia 2013; Rafiee et al. 2022), adaptive neuro-fuzzy inference systems (ANFIS) (Jang 1993; Park et al. 2012; Faryabi 2023), and support vector machines (SVM) (Lee et al. 2018; Mehrnoor et al. 2023; Rajabi et al. 2023). Additionally, various other methodologies such as adaptive neuro-fuzzy inference system–genetic algorithms (ANFIS–GA) (Wen et al. 2022), random forest (RF) (Ebrahimy et al. 2020), and Bayesian logistic regression (BLR) (Tien Bui et al. 2018), have found applications in mapping susceptibility to land subsidence (Eghrari et al. 2023). However, despite their potential, as these models are largely data driven but not physically- or process-based, they rely on the quality and quantity of available data (Bejani and Ghatee 2021). Without sufficient or reliable data, AI and ML models may produce skewed or over-fitted results (Ray 2019).

These models provide physically consistent results of consolidation induced by water pressure changes in aquifer–aquitard systems (Dassargues 2018). In such models, water pressure variations due to groundwater abstraction or recharge change the effective stress in the subsurface, leading to consolidation or uplift. This geomechanical behaviour can be described by elastic or elastoplastic rheological laws, depending on the compressibility of the layers involved. However, significant challenges remain in comparing the outputs of process-based models with PS-InSAR-derived displacement estimations. Conceptual choices in the modelling approach such as the selection of specific storage coefficients, can introduce biases into the simulation results, making it difficult to directly compare model outputs with PS-InSAR estimations. Additionally, discrepancies in spatial resolution, temporal coverage, and data gaps can further complicate these comparisons.

This study addresses these challenges by integrating PS-InSAR data with a 3D groundwater flow model coupled with a 1D geomechanical model in a focused local case study near Antwerp, Belgium. Surface displacements in the region have been detected and mapped since the 1990s using PS-InSAR, providing a valuable dataset for assessing long-term subsidence trends. The four possible drivers of subsidence in the Antwerp region include:

1. The natural consolidation of the Holocene estuarine sediments
2. Additional consolidation due to backfill overload from the 8 m thick embankments along the harbour docks
3. Saturated-unsaturated consolidation of the harbour backfill materials
4. Consolidation due to pore pressure decrease induced by groundwater pumping from the Cenozoic aquifers

In other studies, the presence of backfill, formed from excavated material from the Scheldt River for harbour infrastructure, has been identified as the main reason for subsidence in the Antwerp region (Declercq et al. 2021). In this work, a local area outside the harbour's backfill was selected to focus only on the effects of ground hydraulic head changes on subsidence, excluding the other potential factors. The results from the 1D geomechanical model were compared to the PS-InSAR deformation estimates, projected onto the vertical direction. Rather than calibrating the numerical models to fit the PS-InSAR observations, this approach focuses on assessing whether the deformation trends observed on the surface can be explained using physically based parameters derived from prior studies and in situ tests.

Methodology

Pumping or draining groundwater can lead to the settlement of hydrogeological layers, which in turn may result in land subsidence. This phenomenon has been recognized for many years and can be explained by using the concept of the Terzaghi principle, formulated in 1925 (Terzaghi 1925) for saturated porous media:

$$\sigma = \sigma' + p \tag{1}$$

where σ' is the effective stress, p is the water pressure, and σ is the total stress, all expressed in Pa [$ML^{-1}T^{-2}$]. The effective stress is defined as the 'grain to grain' stress or the stress occurring within the solid matrix of the saturated medium.

Any increase in this effective stress is thus considered the driver of consolidation. A decrease in water pressure in a saturated geological medium induces an increase in effective stress in both confined and unconfined conditions (Dassargues 2018). In confined conditions, the total stress may be considered unchanged, as the pressure decrease through the confining layers is very slow to propagate, and the saturation of the upper layers can be maintained by the recharge from the surface. In unconfined conditions, a portion of the effective stress decrease is balanced by a possible decrease of the total stress by lowering the total saturated column (Dassargues 1995; Dassargues 2018). It is important to note that land subsidence does not necessarily require a partial desaturation of the geological formation. Any decrease in pore pressure, leading to an increase in effective stress, is sufficient to trigger the consolidation process.

Consolidation can be a delayed compaction process because of the slow change of groundwater storage caused by the compressibility of the saturated porous medium under the transient flow and drained conditions. This geomechanical behaviour occurring in the most compressible layers as clayey, peaty, and

loamy loose sediments can most often be described by elastic, elastoplastic, or visco-elastoplastic rheological laws. The viscous component, delayed over time, can also be invoked in the long term and considered as a 'secondary consolidation'.

The volume compressibility of a saturated porous medium is expressed by:

$$-\frac{1}{V}\frac{\partial V}{\partial t} = \alpha \frac{\partial \sigma'}{\partial t} \tag{2}$$

where α is the volume compressibility of the porous medium [Pa^{-1}], the negative sign is justified as a decrease of total volume V [L^3] is expected for an increase in effective stress. An important observation is that volume compressibility is not constant but depends on the value of σ' and thus also on the preconsolidation effective stress σ'_{max} (i.e., the highest effective stress value previously applied to the considered porous medium).

Land subsidence induced by anthropogenic changes in groundwater conditions can be local or regional. The subsiding regions most often correspond to areas where compressible loose sediments are present. Compressible layers are made of recent fluviatile, coastal, estuarine, deltaic, and lacustrine sediments (Poland and Davis 1969). Under certain sedimentological circumstances, they can even be underconsolidated (i.e., at a lower effective stress than the expected one at the considered depth in a saturated column in equilibrium).

A 'compression constant' C and a 'swelling constant' A can be defined as describing the effective stress-strain relationship. These constants are defined in a linearized lnσ', relative deformation) diagram, which shows the presumed elasto-plastic geomechanical behaviour. The 'swelling constant' A illustrates the reversible elastic behaviour (below the preconsolidation effective stress), whereas the 'compression constant' C describes the nonreversible plastic behaviour (above the preconsolidation effective stress; Fig. 1a). Similarly, in a linearized, (logσ', void ratio e) diagram, a compression index C_C and a swelling index are depicted C_S (Fig. 1b). Oedometer tests allow for the determination of those characteristics cited in various studies (Lambe 1951; Jorgensen 1980; Dassargues 2018).

Considering the intrinsic connection between the specific storage coefficient and compressibility values, groundwater literature often distinguishes the elastic and inelastic (plastic) geomechanical behaviours via elastic and inelastic specific storage coefficients (S_{ske} and S_{skv}) (Zhuang et al. 2017; Li et al. 2022a, b).

Using the oedometer test results, the elastic (S_{ske}) and inelastic skeletal specific storage (S_{skv}) coefficients introduced in the 1D-geomechanical model used in this study can be calculated (Hoffmann 2003). First, compressibility α is calculated using the results of oedometer tests in terms of geomechanical parameters (A, C) (Dassargues 2018):

$$\begin{cases} \alpha = \frac{1}{A \cdot \sigma'} & \sigma' < \sigma'_{max} \\ \alpha = \frac{1}{C \cdot \sigma'} & \sigma' \geq \sigma'_{max} \end{cases} \tag{3}$$

Alternatively, if the provided geomechanical parameters are (C_C, C_S):

$$\begin{cases} \alpha = 0.434 \times \frac{C_S}{\sigma'}\sigma' < \sigma'_{max} \\ \alpha = 0.434 \times \frac{C_C}{\sigma'}\sigma' \geq \sigma'_{max} \end{cases} \tag{4}$$

Once the compressibility values α were obtained, the specific storage coefficients can be directly written in relation to volume compressibility (Pa-1) [M^{-1} LT^2] (Dassargues 2018):

$$S_S = \rho g \alpha \tag{5}$$

where ρ is the density of water and g is the acceleration due to gravity. Finally, to obtain the elastic and inelastic skeletal

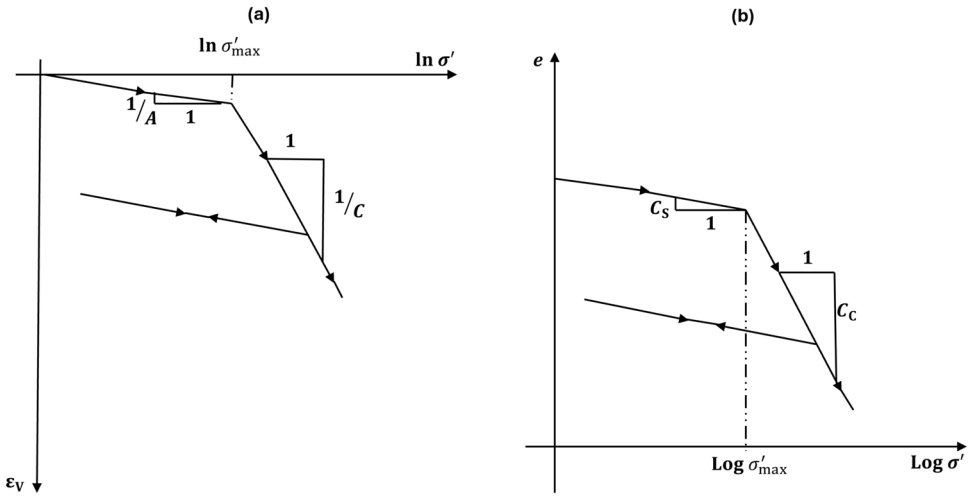

Fig. 1 Diagrams of: **a** relative deformation (ε_V) in function of the natural logarithm of effective stress (lnσ'); **b** void ratio (e) in function of the logarithm of effective stress (logσ') (modified from Dassargues (2018))

storage coefficients for the geomechanical model used in this study, the specific storage values were multiplied by the thickness of each layer b (Hoffmann et al. 2003):

$$\begin{cases} S_{ske} = S_{S(elastic)} \times b\sigma' < \sigma'_{max} \\ S_{skv} = S_{S(inelastic)} \times b\sigma' \geq \sigma'_{max} \end{cases} \quad (6)$$

where S_{ske} and S_{skv} are the inelastic and elastic skeletal specific storage coefficients of each sublayer. In the 1D geomechanical model used in this study, these parameters are crucial for the vertical deformation simulation in each layer. From the pore pressure and effective stress calculated at each time step, a 1D vertical geomechanical model simulates deformations through these equations:

$$\begin{cases} \Delta b = S_{ske} \times \Delta hh < h_{min} \\ \Delta b = S_{ske} \times \Delta hh \geq h_{min} \end{cases} \quad (7)$$

where h is the hydraulic head at a given timestep, and h_{min} is the preconsolidation head corresponding to the maximum preconsolidation stress. To enhance simulation accuracy in modelling subsidence, particularly in this study, compressible layers must be finely discretized into sublayers, maintaining consistent hydrogeological and geomechanical parameters. This fine discretization improves the representation of water pressure distribution within each layer, which is particularly critical for thick, low-permeability layers. Using these principles, subsidence simulations in this study can more accurately capture the time-dependent deformations in hydrogeological materials, reflecting both elastic and inelastic characteristics. This approach provides a comprehensive theoretical background for understanding and predicting land subsidence behaviour effectively, specifically for this study. In this study, the 3D groundwater flow model and the 1D geomechanical model are sequentially coupled. The 3D model computes the spatial and temporal evolution of hydraulic head using MODFLOW, based on prescribed head boundary conditions derived from piezometric maps and a small number of piezometric wells. These simulated heads are extracted at the location of each model cell for all hydrogeological layers and their sublayers, and used as input to the corresponding 1D geomechanical model. Each vertical column then simulates deformation using layer-specific compressibility and specific storage parameters obtained from oedometer test results. The coupling is one-way: deformation does not feed back into the flow model, as the induced subsidence is not expected to significantly change regional hydraulic gradients. This one-way sequential coupling ensures a physically realistic representation of groundwater–deformation interaction while maintaining computational efficiency. A summary of this workflow is shown in Fig. 2.

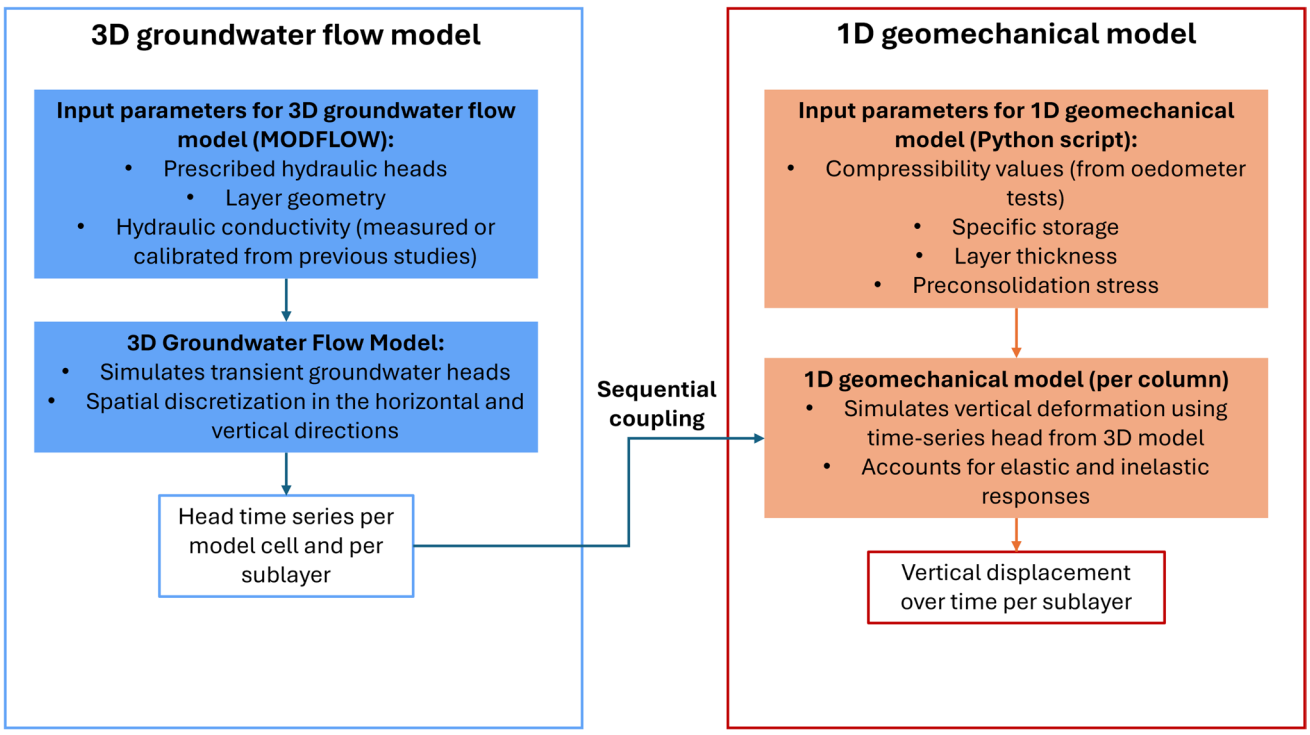

Fig. 2 Schematic workflow of the sequential coupling between the 3D groundwater flow model and the 1D geomechanical model

Study area

Background, model setup and boundary conditions

Land subsidence was studied around Antwerp, the second largest city in Belgium, where surface displacements have been detected and mapped since the 1990s. This monitoring was achieved by employing the PS-InSAR space-based technique on ERS1/2, ENVISAT ASAR, and Sentinel-1A radar data (Declercq et al. 2021; Choopani et al. 2021). As a result, land subsidence measurements are available for this site during the periods between 1992–2001, 2003–2010, and 2016–2023. For this study, high-resolution TerraSAR-X data from 2019 to 2022 were also used. PS-InSAR provides insights into both the spatial extent and magnitude of surface deformation. Displacement magnitudes are presented as LOS velocity over specific observation periods and displacement time series. A global hydrogeological map (Fig. 3) across Belgium and the neighbouring countries is provided. Located on both riversides of the Scheldt, within Antwerp city limits, the harbour has seen progressive development. The elevation in the Scheldt polders varies from 0.5 to 5 m, relative to the Belgium reference altitude (Declercq et al. 2021).

The region lies on low-lying polders in the upper reaches of the Sea Scheldt estuary (Fig. 4). Despite no significant groundwater extraction recorded in the area, subsidence spanning the entire Antwerp region has been observed since 1992 using PS-InSAR. The subsidence rates in the Antwerp city centre differ from those in the harbour installations. In the habour area, land subsidence can be driven by different processes other than groundwater pumping, such as the natural and over-consolidation of Holocene estuarine sediments due to overloading of backfill with 8-m-thick embankments along the harbour docks, and the saturated-unsaturated consolidation of backfill materials (Fig. 4).

To ensure a focused analysis of the subsidence due to changes in water pressure in the aquifers and aquitards, while excluding the effects of compaction of the embankment, it was decided to choose a study area deliberately positioned outside the embankment limits. To understand potential consolidation processes in the most compressible strata (Paleocene and Eocene) arising from pore pressure decreases in various Cenozoic aquifers (Fig. 5), a 3D groundwater flow model sequentially coupled to a 1D-geomechanical model has been developed.

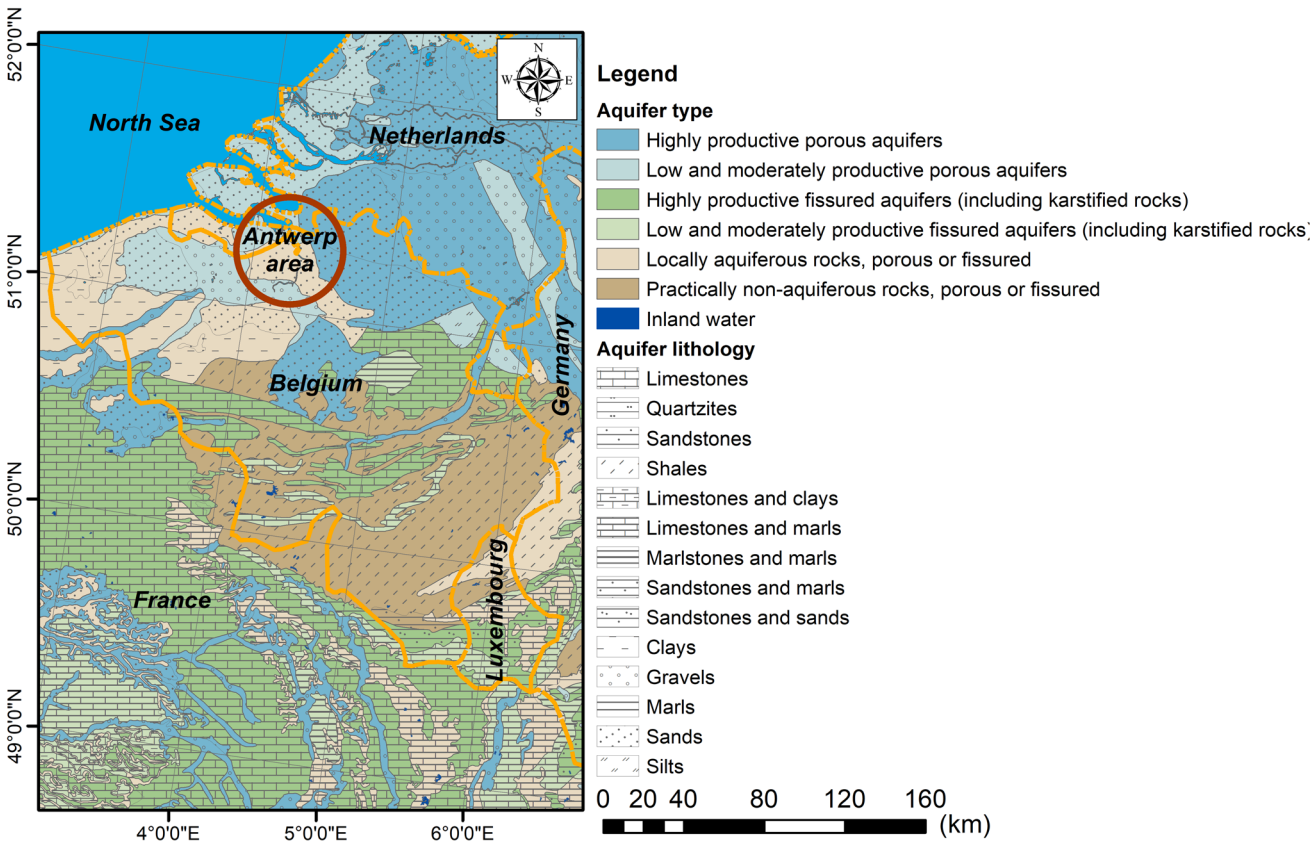

Fig. 3 Hydrogeological location map. Data from the International Hydrogeological Map of Europe at a scale of 1:1,500,000 (IHME1500; BGR and UNESCO 2013)

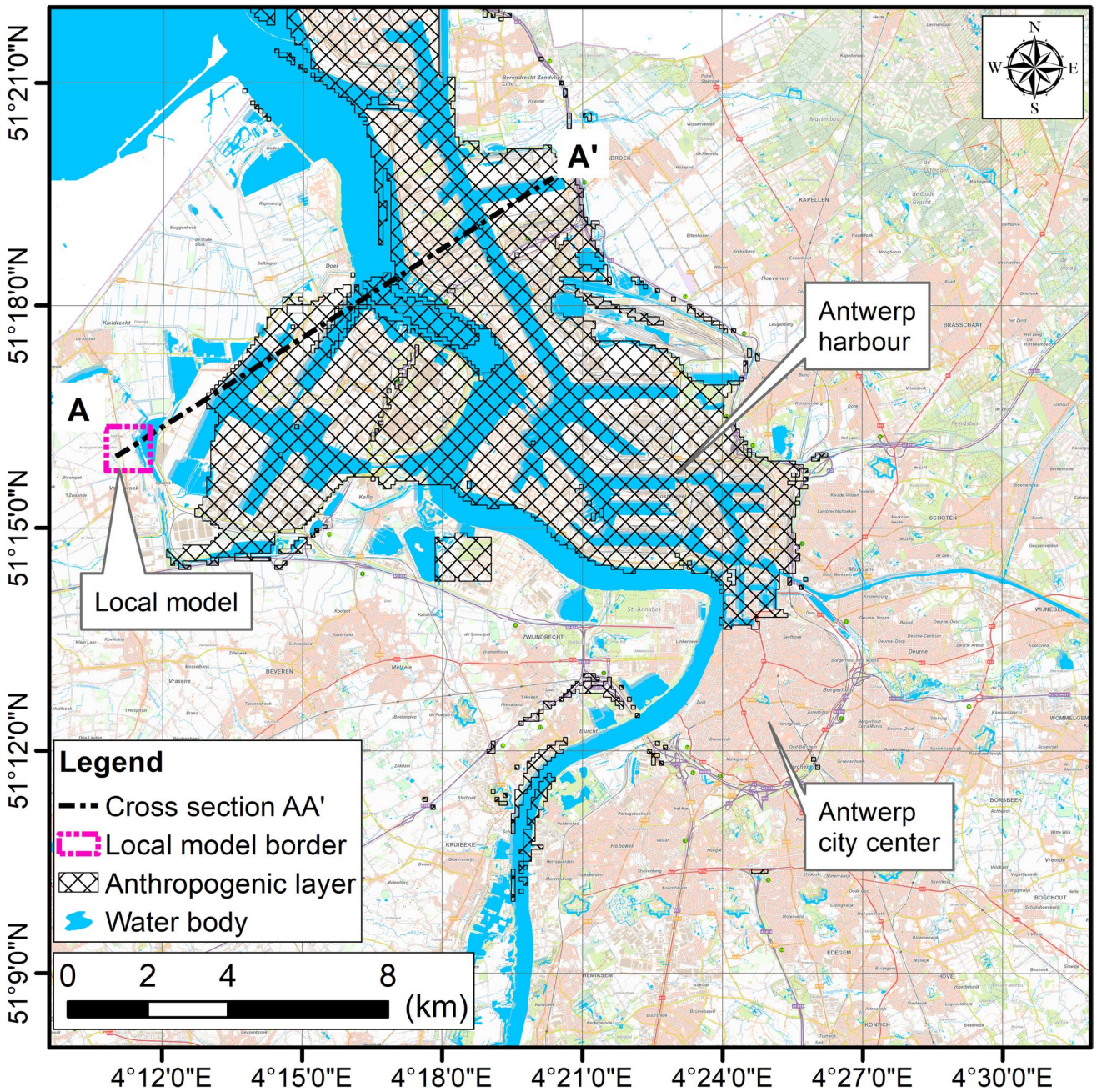

Fig. 4 Location map of the Antwerp region in Belgium. (The border of the Anthropogenic layer is from the Geological 3D model, v3.1; DOV 2024)

This 3D groundwater flow model covers an area of 1.1 km^2 and includes nine layers of loose sediments (Fig. 5). The study area comprises nine main hydrogeological units up to a depth of 225 m. These include four aquifers, four aquitards, and the uppermost layer, composed of mixed sand and clay.

The boundary conditions of the 3D groundwater flow model were prescribed as Dirichlet-type (fixed head) for the aquifer layers and no-flow for the aquitards, based on available piezometric data and hydrostratigraphic interpretation. For aquitard layers, all lateral boundaries were considered as no-flow, as these units act as confining layers and have very low hydraulic conductivity. For the aquifers (layers 2, 4, 6, 8), hydraulic head values were assigned along the eastern and western lateral boundaries, representing regional flow patterns from higher head values in the east toward lower heads in the west. The northern and southern boundaries for aquifers were assumed to be no-flow boundaries as a result of the absence of significant head gradients in those directions observed in the regional piezometric maps. For several aquifer layers where a piezometric observation well was located precisely on the

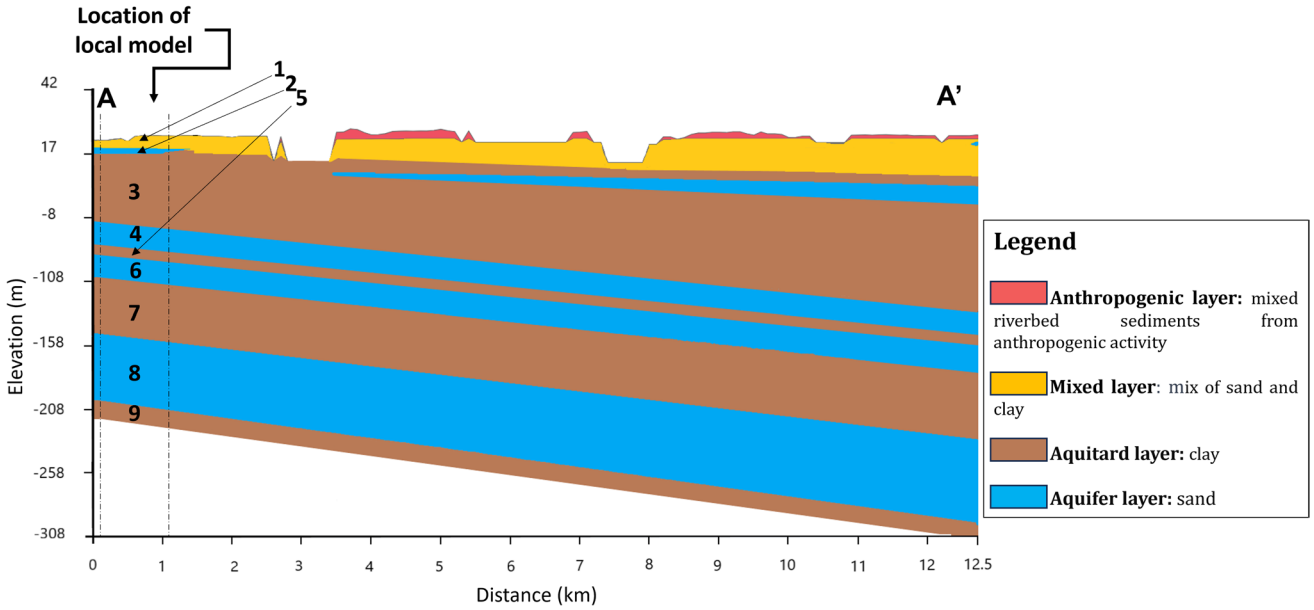

Fig. 5 Simplified hydrogeological cross-section AA′ (as drawn in Fig. 4) showing in depth the interlayering between compressible clayey aquitards and sandy aquifers. Elevation values are given in m and above the Belgian reference level. The numbers shown on each layer represent the corresponding layer number in the model. This cross-section is based on an interpretation of data from the Geological 3D model (v3.1) and the Hydrogeological 3D model (v2.1) available on DOV (2024)

eastern or western boundaries, measured hydraulic head values were directly assigned as a boundary condition. Where piezometric observations were located away from the model boundary, hydraulic head values were estimated by projecting the values from piezometric maps using linear interpolation between observation wells and the model boundaries.

The uppermost layer (layer 1) is the Quaternary layer, including polder deposits, characterized by mixed sand and clay. Below this (layer 2) is the Pleistocene and Pliocene aquifer system, which actually forms part of the broader Miocene aquifer and consists primarily of sandy deposits. Layer 3 is Boom Aquitard, composed of clay, which acts as a confining unit. Layer 4 is the Ruisbroek-Berg Aquifer, also known as the Upper Oligocene Aquifer, featuring sandy materials, while layer 5 is the Tongeren Aquitard, another significant confining layer rich in clay. Layer 6 is the Lower Oligocene Aquifer, composed of sandy sediments, and layer 7 is the Bartoon Aquitard System, characterized by its clay composition, whereas layer 8 is the Ledo-Paniselian-Brusselian Aquifer System, consisting of mixed sand and clay. Finally, Layer 9 is the Paniselian Aquitard System, the deepest unit, mainly composed of clay.

For groundwater modelling, accurate information regarding the geometry and the hydrogeological properties of the different layers is needed. The simulation of groundwater flow and consolidation processes necessitates values for the key parameters such as the horizontal hydraulic conductivity (K_h), the vertical hydraulic conductivity (K_v), and the specific storage (S_s) of each layer. Data about the source/sink of groundwater such as groundwater abstraction rates and recharge, also play an important role. The hydrogeological characteristics of aquifers and aquitards can be assessed using various techniques; however, this falls outside the scope of this paper. In situ measurements such as pumping and recovery tests data are usually only available in aquifers. For aquitards, lab-scale measured data based on permeameter and oedometer tests, but are only available with exception. As a result, first-guessed values for those parameters are often based on estimations gathered from the literature (Dassargues 2018) on the basis of the identified lithologies. The main problem is, however, that a large uncertainty usually remains for these values of parameters, which is only partially solved by calibration of the model on measured data. The reliability of the calibration depends, then, strongly on the availability of historically measured potentiometric heads in each aquifer and in different locations.

In the study conducted in Antwerp, significant challenges arose resulting from data scarcity. For several layers, hydraulic conductivity parameters are derived either from direct measurements or from prior calibrations documented in other studies, as detailed in Table 1 (Gedeon et al. 2007). Most hydraulic conductivity values were inferred from grain size distribution analysis, occasionally supplemented by pump or slug tests. Two potentiometric maps were available in Antwerp: one for the Miocene aquifer (Labat 2011) (layer 2) and another for the Oligocene aquifer (2009) (layers 4 and 6; Vandersteen et al. 2012; Vlaamse Milieumaatschappij 2016). As the deeper aquifers are characterized by a high salt content, they are less exploited than the shallow layers, which offer reserves of high-quality groundwater (Vandersteen et al. 2012). In the

Table 1 Values of vertical and horizontal hydraulic conductivity in different layers used for the Antwerp local model, derived from various sources including the central Campine model (Verbeiren et al. 2006), Brulandkrijt model (Ministerie van de Vlaamse Gemeenschap 2004), and direct measurements (Vandersteen et al. 2012)

Layer	K_h(m/s) [a]	K_v(m/s)	K_h and K_v source locations
1	1.5×10^{-5}	3.0×10^{-6}	Central Campine model
2	6.5×10^{-5}	1.3×10^{-6}	Central Campine model
3	3.8×10^{-9}	1.7×10^{-10}	Brulandkrijt model and Central Campine model
4	2.7×10^{-5}	6.7×10^{-6}	Brulandkrijt model
5	1.8×10^{-10}	5.4×10^{-11}	Measured
6	2.3×10^{-6}	2.3×10^{-8}	Brulandkrijt model
7	1.2×10^{-11}	1.2×10^{-13}	Brulandkrijt model
8	4.1×10^{-5}	1.0×10^{-5}	Brulandkrijt model
9	1.2×10^{-9}	1.2×10^{-11}	Brulandkrijt model

[a]For model layers that combined two zones with similar lithology, a geometric mean of their values was calculated to obtain a single representative value for each unified layer. Furthermore, where the literature provided two calibrated values from different models for the same layer, the geometric mean was also calculated. In cases where a range of values was provided, the geometric means of these ranges were determined

broader Antwerp region, the Miocene aquifer system experiences, thus, significant pumping activity. However, this aquifer was not being exploited locally within the area of this study's local model. On the contrary, within the Oligocene aquifer, a pumping well in the centre of the local model area with an extraction rate of 2,800 m^3/year is taken into account within the Oligocene aquifer. The layer corresponds to layer 6 (Lower Oligocene Sandy Aquifer) of the model (Fig. 4). Given the limited availability of data on groundwater levels and fluxes, calibration of the model and optimization of the parameters were considered inappropriate within the scope of this research, and the model was mainly constrained by boundary conditions. Table 1 provides the values used here, derived from the available data.

The geotechnical parameters used in this study were derived based on the principles outlined in section 'Methodology'. In the local model, the assessment of geotechnical parameters was based on thorough reviews of geotechnical reports and studies. For the shallow layers, tested samples from four boreholes, located near the eastern boundary of the local model (Geotechnics Department in Flanders 1999) were analyzed to derive C and A. For the deeper low-permeability layers, comprehensive geomechanical studies conducted in the region (i.e. Kallo, Mol, and Essen), together with hydrogeological reports, have provided C_C and C_S index values (Deng et al. 2011; Nguyen et al. 2014). For the sandy aquifers corresponding to layers 4, 6, and 8 (Fig. 4), the same geomechanical parameters were used as those of the sandy layer 2, a shallow layer for which there was direct borehole data. This decision was based on similarities in the lithology between them, even though both their depths and thicknesses differed significantly. Additionally, it also considered the same parameters for layer 5, a deep clay aquitard, as was done for Boom Clay (layer 3). For layers 7 and 9, corresponding to the deep clay aquitards, characteristics similar to those of the Ieperiaan clay (Nguyen et al. 2014) were chosen.

Further, the preconsolidation effective stress (σ'_{max}) for the uppermost layer was assumed based on the current potentiometric head at the initial date of simulation, representing a normally consolidated state, implying that the uppermost layer behaves inelastically as it adjusts to changes in stress. For the deeper overconsolidated layers, the preconsolidation effective stress is considered the equivalent to the potentiometric head of 50 m below the current head in each layer. This reflects sedimentary paleo loading and unloading events, implying a state of overconsolidation. Consequently, these

Table 2 Elastic and inelastic skeletal storage coefficients for each model layer. These values are calculated from oedometer test results conducted on samples from four boreholes on the eastern boundary of the local model (Geotechnics Department in Flanders 1999), Essen and Mol (Deng et al. 2011), and Kallo (Nguyen et al. 2014)

Layer	S_{ske}(-)	S_{skv}(-)	A and C source locations	C_S and C_C source locations
1	3.0×10^{-3}	2.3×10^{-2}	Eastern boundary boreholes	-
2	3.5×10^{-3}	2.1×10^{-2}	Eastern boundary boreholes	-
3	3.5×10^{-2}	8.0×10^{-2}	-	Essen and Mol
4	9.2×10^{-4}	5.3×10^{-3}	Derived from similar lithology (see layer 2)	-
5	2.3×10^{-3}	5.1×10^{-3}	-	Derived from similar lithology (see layer 3)
6	8.3×10^{-4}	4.8×10^{-3}	Derived from similar lithology (see layer 2)	-
7	1.5×10^{-2}	4.4×10^{-2}	-	Similar to Ypresian clay in Kallo[a]
8	1.1×10^{-3}	6.3×10^{-3}	Derived from similar lithology (see layer 2)	-
9	2.7×10^{-3}	8.1×10^{-3}	-	Derived from similar lithology (see layer 7)

[a]For layer 7, data sourced from Ypresian clay samples in Kallo is used because of its lithological similarity and comparable depth characteristics, although it is not directly part of the modelled layers

deeper layers exhibit elastic behaviour when the effective stress is below this historical maximum and inelastic behaviour when it exceeds this threshold. In summary, geotechnical data from diverse sources with inherent assumptions were adopted. Indeed, uncertainties for these values are large as a result of data limitations and lithological variability. Table 2 lists the values for both elastic and inelastic skeletal storage coefficients across the layers of the model considered for the geomechanical computations. They are the best approximations based on existing data and limitations.

Layer discretization and delayed consolidation response

In most numerical models, the water pressure variation is assumed linear within one finite element or one

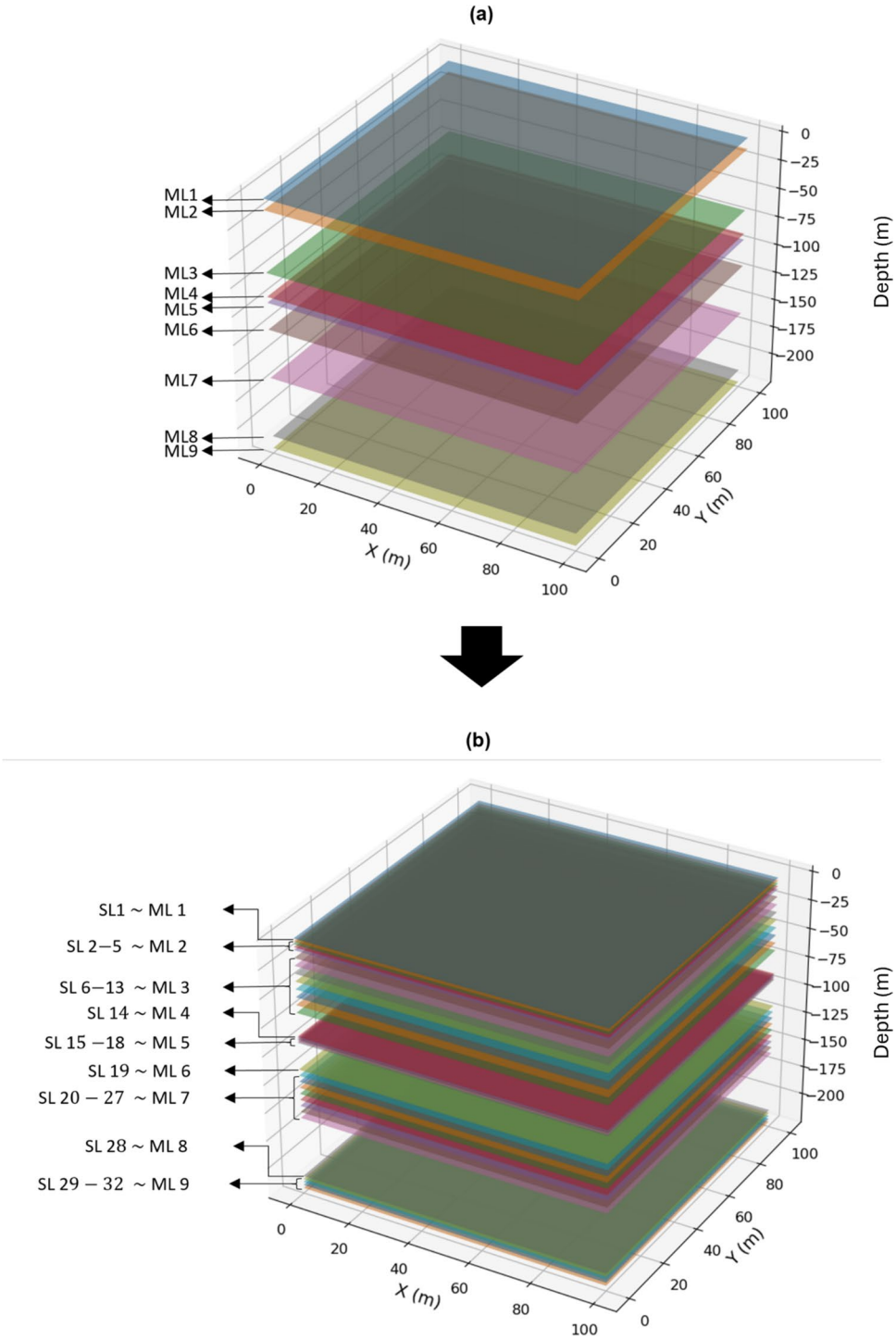

Fig. 6 3D visualization of the hydrogeological model with only the main layers (MLs); **b** with the finer discretization in sublayers (SLs)

finite-difference cell. This induces an unrealistic approximation of the pore pressure in the aquitard compressible layers if they are modelled by one layer of cells or elements. To obtain a better approximation of the vertical distribution of the pore pressure, the compressible layers must be discretized with finer sublayers. Thus, using MODFLOW, the discretization of main layers (MLs) into finer sublayers (SLs) enhances the accuracy of simulations, even if these SLs are given the same hydrogeological and geomechanical parameters. This finer vertical resolution is particularly critical for thick low-permeability layers, which are more susceptible to delayed consolidation resulting from slower pore-water pressure dissipation in the low-permeability and compressible layers. By subdividing layers (i.e., in this case, layer 2 into four units, layer 3 into eight, layer 5 into four, layer 7 into eight, and layer 9 into four), finer vertical resolution was achieved (Fig. 6). The increased number of SLs enables the simulation to approximate the delay in deformation that is observed in hydrogeological materials exhibiting elastic or inelastic characteristics. This discretization captures the delayed consolidation response: pressure drops in low-permeability sublayers propagate gradually, inducing delayed compaction. Without such vertical subdivision, in MODFLOW's finite-difference framework, each cell or layer is treated as hydraulically uniform (head changes are assumed to be linear and therefore propagate instantaneously across the full thickness), so a coarse single-layer model enforces immediate compaction and entirely omits the diffusion-driven delay that is characteristic of low-permeability strata. Through this discretized layering, the model can more accurately simulate deformation over time in each SL and eventually each ML of the local model.

MODFLOW simulations were conducted to compute hydraulic head dynamics across these adjusted SLs. The simulation spanned from 2007 to 2023, providing temporal evolution of the hydraulic head, which is used as input for deformation calculations. Hydrogeological and geomechanical parameters were maintained across the SLs, with values corresponding to their original ML.

From the pore pressure (and thus the induced effective stress) calculated at each time step and in each sublayer, a 1D vertical geomechanical model is used to simulate the deformations. The script developed in this study calculates incremental deformation (Δb) at each time step, for each sublayer, following the rules introduced in section 'Methodology'.

The script compares h and h_{min} at each timestep and determines the type of deformation (i.e., inelastic or elastic): the initial h_{min} for sublayer 1 was set to the initial head at the start of the simulation and for the other layers, an overconsolidation corresponding to an equivalent head drop of 50 m below the initial head is considered, leading to only elastic deformation.

Results

Land subsidence estimations

The most recent deformation measurements in Antwerp were obtained using the Stanford Method for PSs (StaMPS) time series analysis software (Hooper et al. 2007; Hooper 2008). StaMPS integrates the principles of PS-InSAR into its methodology. The spatial variability and temporal evolution of displacement in the region were determined using data from the ERS (1992–2001; Fig. 7a), Envisat (2003–2010, Fig. 7b), and Sentinel-1A (2016–2020) satellites (Declercq et al. 2021). For this research, the Sentinel-1A data were extended to cover up to 2023 (Fig. 7c). Additionally, TerraSAR-X data from 2019 to 2022, processed using the SARPROZ software (Perissin et al. 2011), were also used to complement the analysis. For this study, only the time series of deformation from TerraSAR-X data during 2019-2022 were used to compare with the results of deformation from the geomechanical model. Annual average velocity maps along LOS from TerraSAR-X data are not depicted in Fig. 7 and will be detailed in a separate study.

For each satellite operational duration, an InSAR time-series data stack for Antwerp was processed to offer a reliable displacement time series spanning 1992–2023. In the central region of the Antwerp harbour, measurements integrated over specific periods provided estimations of land subsidence. For the intervals 1992–2001, 2003–2010, and 2016–2023, the highest estimated average subsidence located approximately in the middle of the harbour was –4.4, –4.1 and –7.4 mm ± 0.49 mm, respectively, along LOS. The city centre of Antwerp, situated on the eastern bank of the Scheldt River, exhibited relative stability with average displacement rates of 0.2 mm/year during 1992–2001, –0.1 mm/year during 2003–2010, and 0.2 mm/year during 2016–2023. These values are relative to a selected reference point, which is crucial for calculating relative movements, as PS-InSAR measures changes in distance between the satellite and the Earth's surface rather than absolute displacements. For the ERS data, a different reference point was chosen, located outside the Antwerp region, while the reference points for the Envisat and Sentinel stacks were situated closer to the city. Despite the differences in their locations, all reference

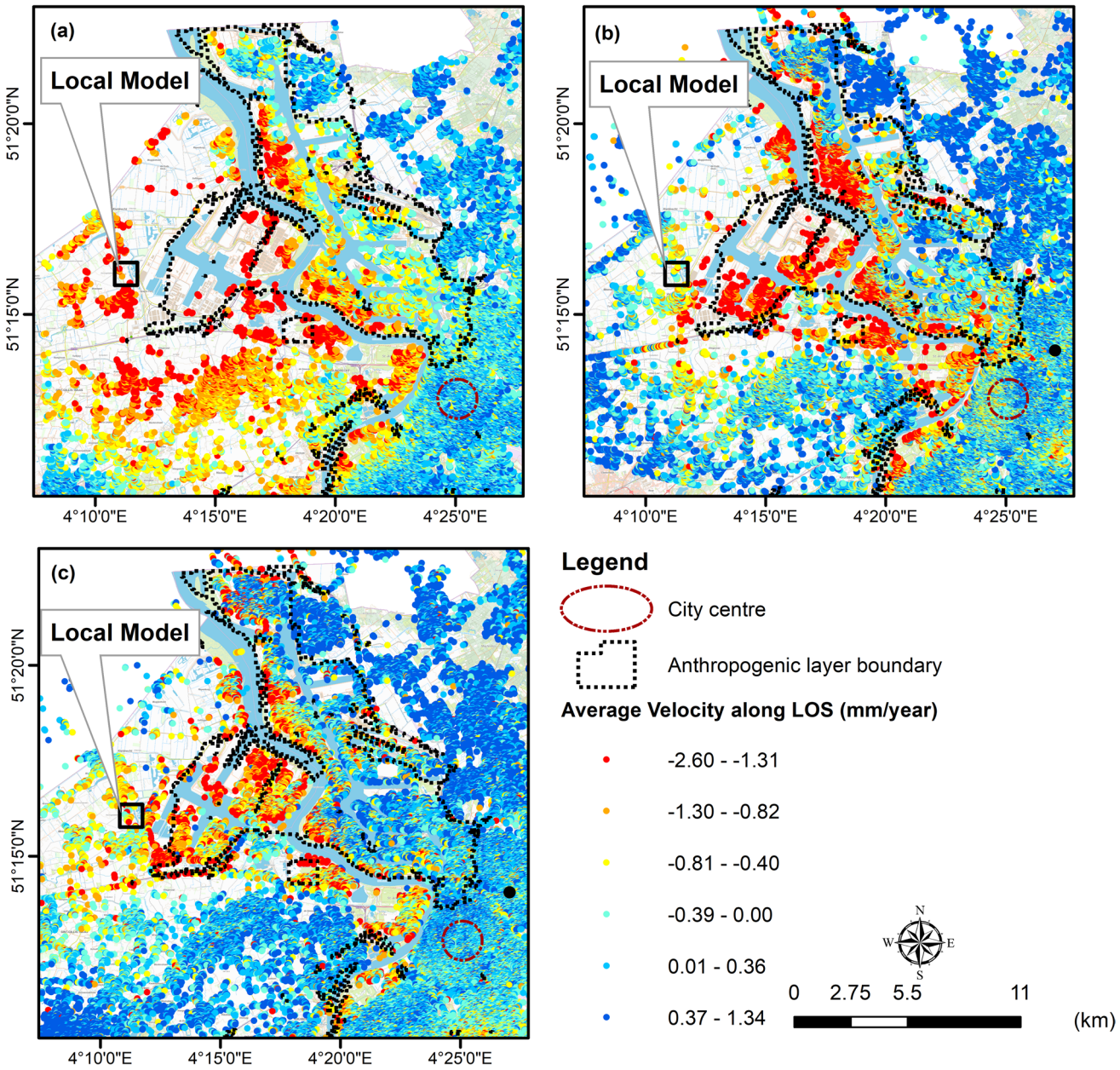

Fig. 7 Annual average velocity map along line of sight (LOS) observed by: **a** ERS (1992–2001); **b** ENVISAT (2003–2010) data from (Declercq et al. 2021); and **c** Sentinel (2016-2023) radar data

points were geologically selected from areas assumed to be stable because of their composition of old, consolidated sediments. In summary, various methods have captured the Antwerp land subsidence patterns over the years. To explain the causes of such displacements, the subsequent section will explore the hydrogeological data.

Hydraulic head evolution

A 3D groundwater flow with the hydrogeological setup of this study area, which is situated on the southwestern border of Antwerp, specifically outside the harbour backfill. Piezometric heads were monitored from 2007 to 2016 using

observations from three piezometric monitoring wells. At the lateral boundaries of the aquifer layers, hydraulic head values were prescribed, while for the remaining low-permeability boundaries, a no-flow condition was considered. Hydrogeological parameters were gathered from past studies conducted in this part of Flanders, and each layer was considered as homogeneous. A regular grid was used in the horizontal plane, consisting of 110 × 110 cells, each with an area of 10 × 10 m. Along the vertical plane, cell dimensions varied based on the thickness of each SL.

To address the delayed responses in deformation, the nine main layers (MLs) were subdivided into 32 sublayers (SLs). The evolution between 2007 and 2023 of the hydraulic head across SLs corresponding to each ML is illustrated through nine subplots (Fig. 8). The uppermost SL (ML 1), composed of a mix of sand and clay, shows hydraulic

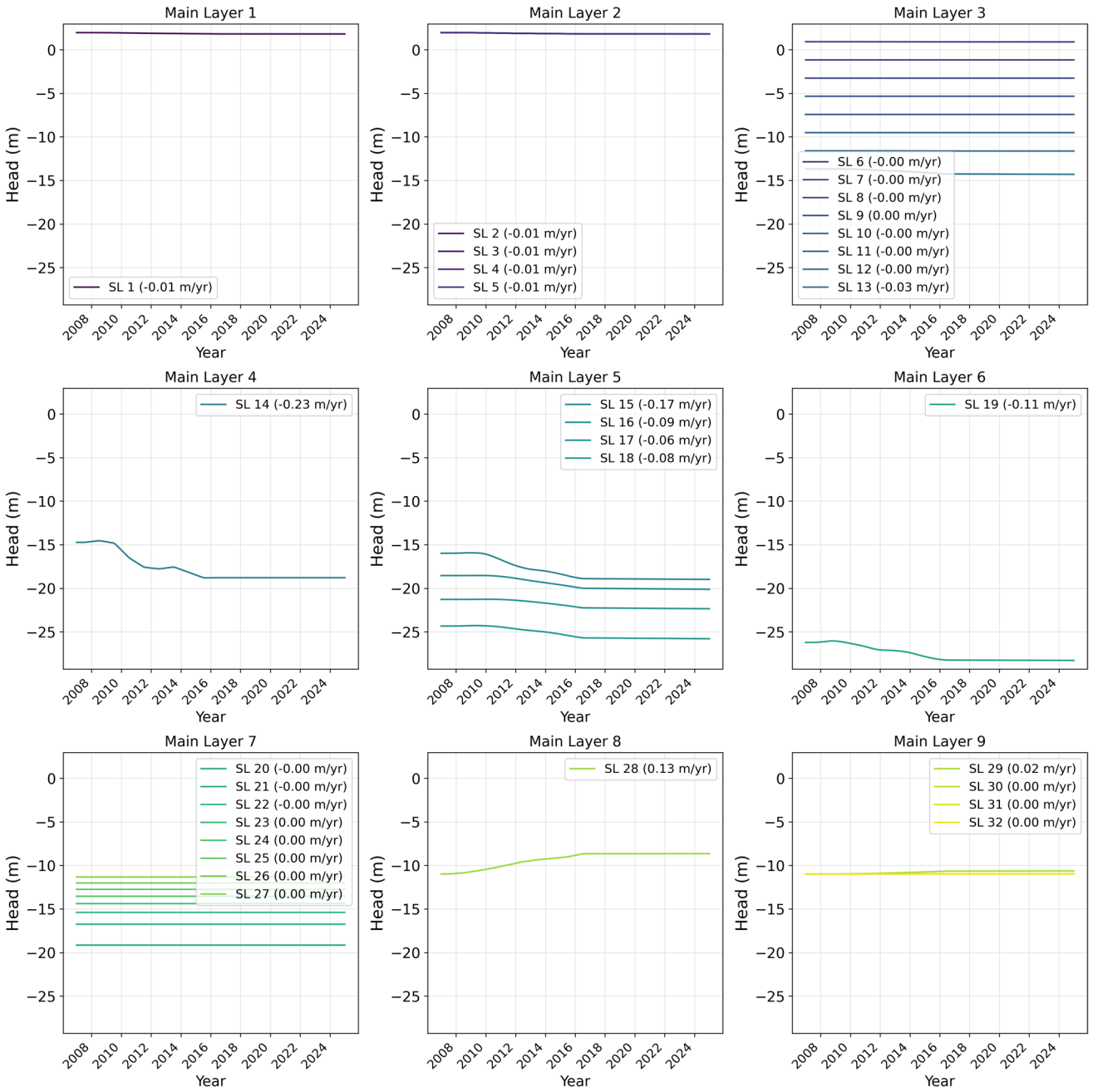

Fig. 8 Temporal evolution of water head across different sublayers of 3D-flow transient simulation, spanning 2007–2023. The rates of change for each layer are indicated in meters per year (m/year)

head fluctuations similar to those observed in ML 2, which includes four SLs classified as an aquifer. This similarity is attributed to the identical boundary conditions applied for both MLs, an assumption was made because of the lack of direct piezometric data for ML 1, assuming that the hydrogeological influences are comparable to those affecting the adjacent aquifer. ML 3, as a low-permeability aquitard, reveals stability of the hydraulic heads over time across its sublayers (SL 6–13), isolating the overlying aquifer (ML 2) from deeper hydrogeological influences. The base of ML 3 (SL 13) exhibits a minor but consistent decline in hydraulic head, decreasing at a rate of –0.03 m/year. This subtle change is attributed to the hydraulic gradient induced by lower prescribed heads in the adjacent ML 4. ML 4 is a dynamic sandy aquifer experiencing the highest change, showing a hydraulic head drop at a rate of –0.23 m/year linked to groundwater abstractions or natural drainage processes within the aquifer.

The influence of the aforementioned dynamic aquifer above ML 5, which is an aquitard, begins to be moderated as evidenced by the decreasing hydraulic head declines from the uppermost SL 15 at –0.17 m/year to deeper SLs, showing reductions to –0.09 and –0.06 m/year, respectively. The computed hydraulic head decline in SL 18 to –0.08 m/year, reversing the previous downward trend, suggests an influence from the aquifer conditions of ML 6 below. In ML 6, the rate of decline in the hydraulic head is –0.11 m/year, depicting less variation than in the aquifer ML 4. In aquitard ML,7 hydraulic heads are stable over time across the SLs. The hydraulic head increases from higher elevation SLs to lower ones (from SL 20 to SL 27) because of the head gradient between the adjacent aquifers ML 6 and ML 8. The aquifer ML 6 exhibits a decline in hydraulic head (–0.11 m/year), creating less downward pressure, while aquifer ML 8, with a rising hydraulic head (+0.13 m/year), exerts more upward pressure on the lower sublayers of aquitard ML 7. The rising hydraulic head in ML 8 is likely due to the cessation of pumping wells that were active in the past, allowing for the recovery of the hydraulic heads. ML 9 (SLs 29–32), as the base of the model, is classified as a low-permeability aquitard. The slight increase in hydraulic head (+0.02 m/year) observed in the uppermost SL 29 is attributed to the influence of the aquifer ML 8 above, which imposes an increasing head. In contrast, the deeper SLs (SLs 30–32) show almost no change because of their depth and the aquitard properties.

Pore pressure distribution across model layers

Figure 9 illustrates the distribution of pore pressure as a function of depth in one vertical column in the centre of the local model. The graph shows the logical pore pressure increase with depth. In MLs 1, 2, 3, and 7, pore pressure profiles remain stable over time. The last SL of ML 3 shows evolving lower water pressures with time, reflecting its interaction with the aquifer pressures in ML 4. The aquitard ML 5 similarly exhibits evolving lower pressures, indicating significant pressure changes driven by lower hydraulic heads in aquifer ML6. Because of its position between aquifers ML 4 and ML 6, a strong hydraulic gradient is created. In contrast, ML 8 shows a slight increase in pore pressure over time, indicating rising hydraulic heads. Stable and consistent pore pressures are computed in ML 9, with hardly any variation over time.

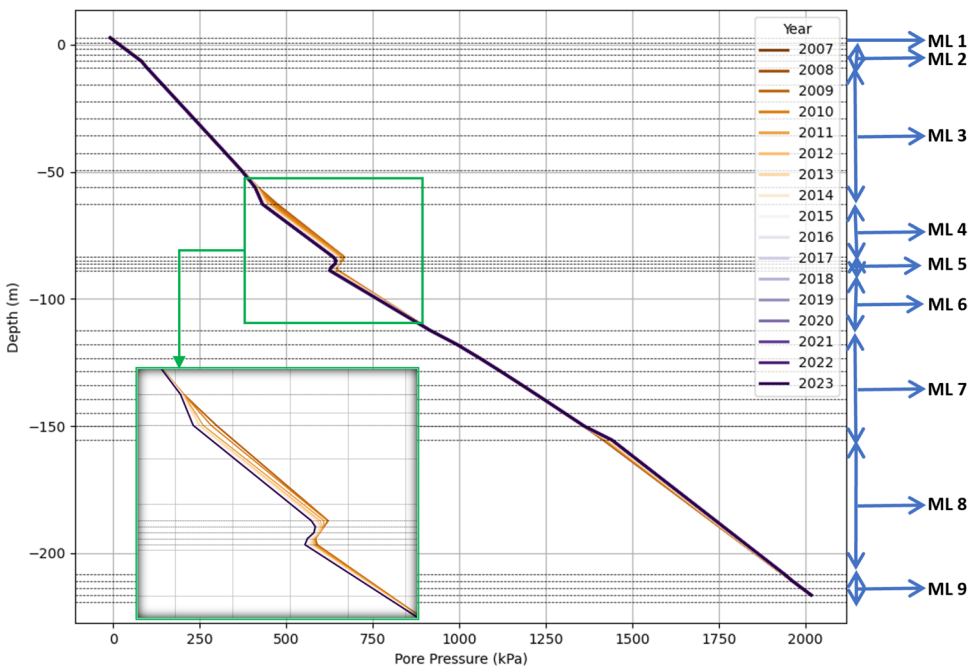

Fig. 9 Pore pressure distribution with depth in a 1D vertical column. Each line on the graph represents the pore pressure profile for a specific year, from 2007 to 2023

Computed deformation across model layers

The variations in deformation are linked to the geomechanical properties and hydraulic head fluctuations within each ML and SL. Figure 10 presents the deformation time series computed across the SLs within each ML during the simulation period. In ML 1, the deformation rate of –0.39 mm/year is significantly high compared to other layers, despite only slight hydraulic head variation. This shows the effect of the inelastic storage coefficient, which is higher than the elastic storage coefficient. As this uppermost layer is considered normally consolidated, even minor head changes lead to inelastic compaction, resulting in disproportionately high deformation compared to deeper overconsolidated units.

In contrast, each SL of ML 2 shows a negligible elastic deformation of –0.01 mm/year despite a similar hydraulic head variation as in ML 1. In ML 2 and deeper, deformation is only elastic. ML 3 exhibits minimal deformation across its sublayers (SL 6–13), except for the sublayer closest to ML 4 (SL 13). Very low deformation rates in the SLs of ML 3 are consistent with their stable hydraulic

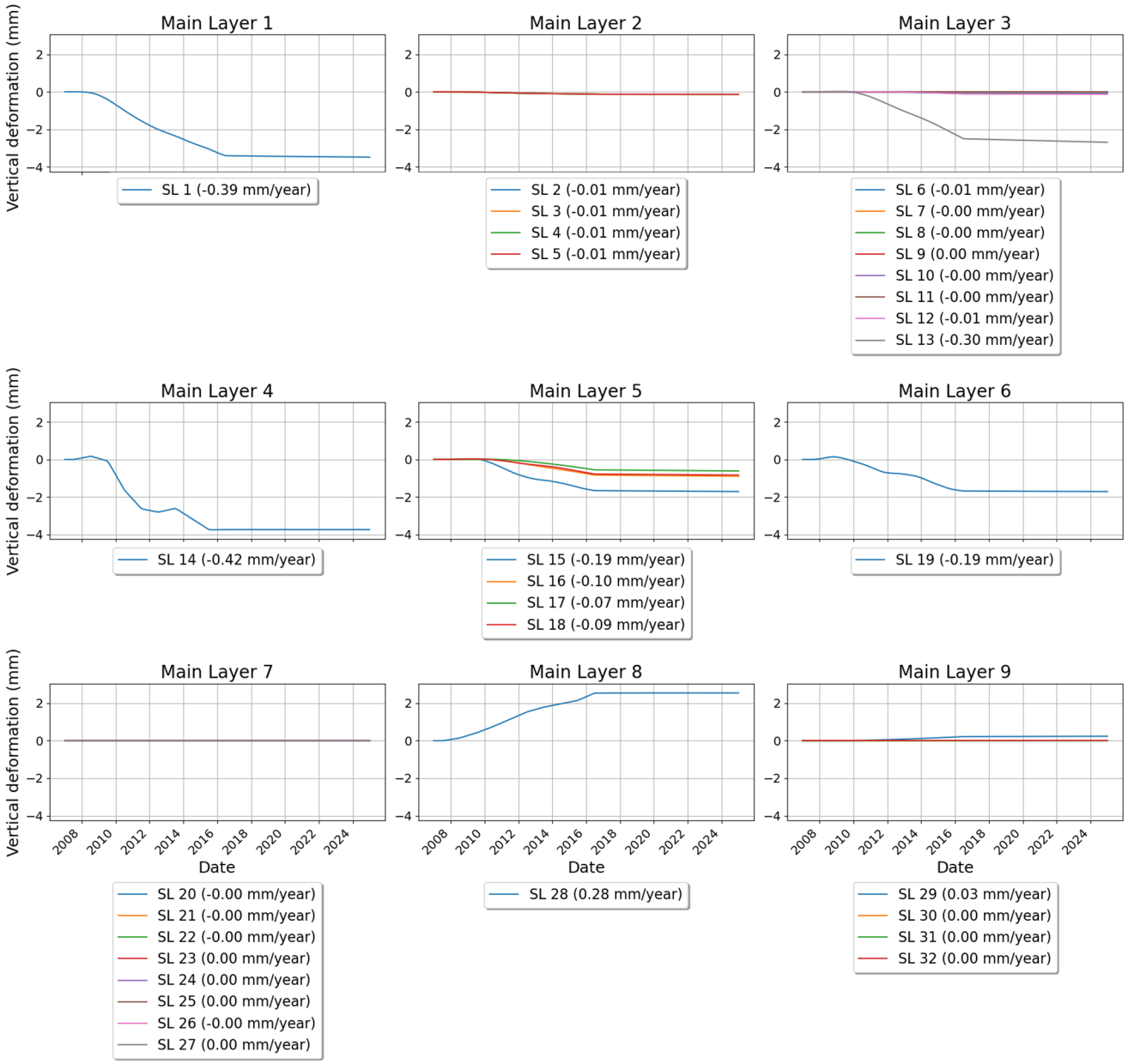

Fig. 10 Temporal evolution of deformation (in mm/year) across different sublayers of the 1D-geomechanical model, during the 2007–2023 period

head over time. In the deeper part of ML 3 (SL 13), a slight deformation is computed at a rate of –0.3 mm/year, induced by the lower heads in ML 4.

Although this rate of displacement is minimal, the Boom clay in this layer has high compressibility and low permeability, making it highly sensitive to even small changes in water pressure. This means that a very negligible water pressure drop can result in significant deformation, leading to a total displacement of up to 2 mm over the period 2007–2016. ML 4 shows the highest rate of deformation, with a deformation rate of –0.42 mm/year, corresponding to a significant rate of hydraulic head decline. This aquifer is primarily composed of sand with shells and glauconite, explaining its compaction. In ML 5, deformation rates decrease with depth: the uppermost SLs (SL 15) exhibit a rate of –0.19 mm/year, reducing to –0.10 mm/year in the middle of ML 5, and further to –0.07 mm/year in the deeper SL. The deformation rate of –0.09 mm/year in SL 18 illustrates the effects of the influence of aquifer ML 6 below. ML 6 shows a moderate deformation rate of –0.11 mm/year, as the hydraulic head is declining. ML 7, another aquitard, shows no deformation across SLs 20–27 because of its stable hydraulic heads over time, preventing the experience of deformation. In ML 8, rising hydraulic heads at a rate of +0.13 m/year lead to a swelling of +0.28 mm/year rather than compaction. Finally, ML 9 at the base of the model, shows minimal deformation because of its stable hydraulic head over time. While SL 29 shows a slight swelling of 0.03 mm/year, influenced by the upward pressure from the upper ML 8, this deformation is too small to be significant. Overall, negligible deformation is computed in ML 9.

Comparison between 1D geomechanical results with PS-InSAR estimations

Figure 11 shows a comparison between computed vertical deformation values from the 1D geomechanical model sequentially coupled to the 3D groundwater model (specifically plotted for the central cell of the model) and deformation values projected onto vertical direction estimated by PS-InSAR estimations across different periods. The PS-InSAR data, extracted from four PS-InSAR data processed in this study, SkyGeo, and EGMS, represent the average time series of PS points located within the limits of the local model area, rather than single PS points. This averaging approach ensures a more reliable and representative comparison by mitigating the effects of local anomalies and measurement noise that could affect individual PS points. The PS-InSAR estimations are relative time series of the deformation. For visualization purposes, the initial values of the Envisat, Sentinel, and TerraSAR-X time series were aligned with the ERS trendline.

Despite the unclear trends of PS-InSAR estimations during data gaps, this provides a practical solution for visualization and allows for simultaneous comparison of deformation rates across the datasets. Computed deformations in the

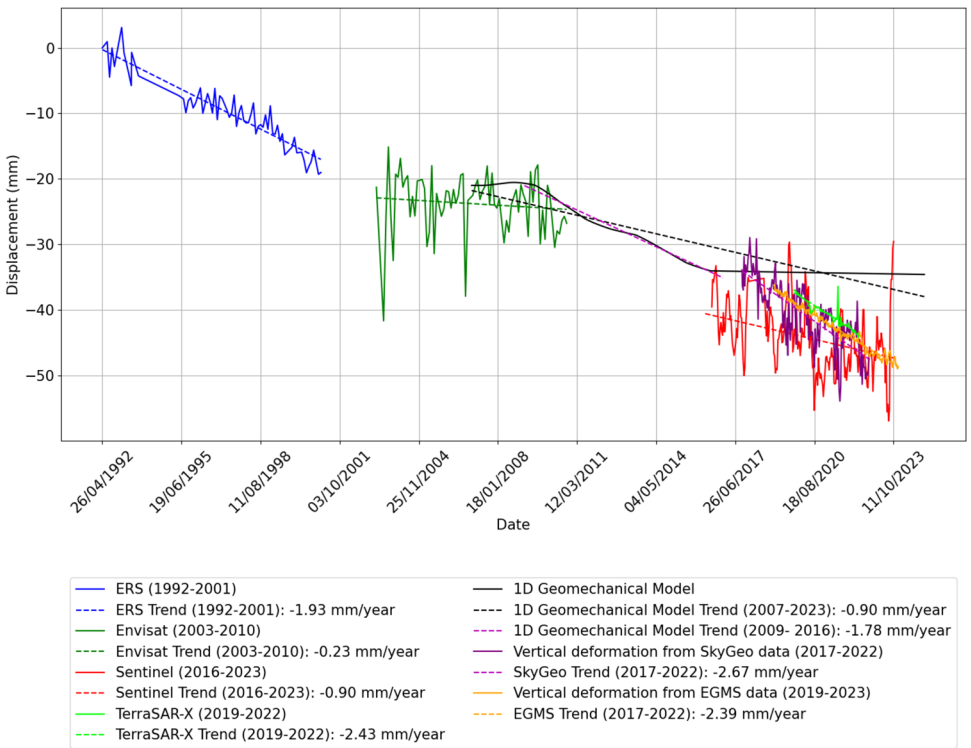

Fig. 11 Comparison between PS-InSAR estimations of deformation values projected onto the vertical direction from different datasets, and simulated deformation from the 1D geomechanical model sequentially coupled to the groundwater model

Table 3 Statistical agreement metrics between simulated deformation from the 1D geomechanical model and PS-InSAR deformation time series for each dataset

Dataset	RMSE (mm)	R^2	MAE (mm)	MBE (mm)	Pearson correlation coefficient
EGMS	1.26 mm	0.867	1.01	0.74	0.987
SkyGeo	3.47	0.521	2.65	0.86	0.786
TerraSAR-X	1.29	0.617	0.92	–0.86	0.921
Sentinel processed by StaMPS	6.54	–0.581	5.5	4.13	0.392

model were also shifted vertically to allow the comparison. PS-InSAR data provide deformation estimations along the LOS of the satellite, which were converted to vertical deformation for comparison purposes.

While the ERS data offers historical insight into subsidence from 1992–2000, showing a trend of −1.9 mm/year, it does not overlap with the deformation phase simulated in the geomechanical model (i.e., post-2007), limiting long-term comparisons. Similarly, the Envisat data, spanning from 2003 to 2010, only have 3 years in common with the modelled time series and indicate a rate of –0.3 mm/year, which falls within the noise level. The early stage of the model, 2007–2009, is not considered reliable as the model is too dependent on initial conditions during the first years of the simulation. PS-InSAR data were unavailable from 2010 to 2016. Post-2016, both the model and PS-InSAR provide time series, but the model results are based only on quite uncertain water pressure induced by a single pumping well with a nearly insignificant discharge rate, rather than on head values from measured piezometric data, which were unfortunately not available during this recent period anymore. All these data issues affect the comparison reliability and interpretation. Concerning PS-InSAR data processing, the Sentinel data periods are not entirely aligned: our processing through ISCE-STAMPS covers 2016–2023 (green), while SkyGeo and EGMS data span 2017–2022 and 2019–2023 (purple and orange, respectively). The Sentinel data processed by SkyGeo and EGMS exhibit low noise and clear deformation rates, complementing the results from the processing. Additionally, the processing of TerraSAR-X data through SARPROZ for 2019–2022 shows a rate of –2.43 mm/year similar to those estimated by SkyGeo and EGMS.

From 2009 to 2016, the 1D geomechanical model shows a rate of –1.78 mm/year, which falls between the vertical deformation rates observed from PS-InSAR estimations (excluding the nonreliable 2007–2009), closely matching the SkyGeo, which shows a slightly higher rate of –2.67 mm/year and is similar to EGMS data from the same period showing –2.78 mm/year. Later, from 2016 to 2023, deformations computed by the model are probably underestimated, as these results are based on incomplete recorded pumping data (as mentioned previously). The TerraSAR-X data processed in this study, covering 2019–2022, show a deformation rate of –2.43 mm/year, which aligns closely with the estimates from SkyGeo and EGMS. The Sentinel data processed through ISCE-STAMPS, show a lower rate of –0.90 mm/year during 2016–2023. These variations can be attributed to differences in processing techniques, regional factors, and the inherent limitations of InSAR as an estimation method.

To quantitatively assess the match between the modelled and estimated PS-InSAR deformation time series, several statistical evaluation metrics were computed. However, since the 1D geomechanical model simulates vertical compaction from 2007 to 2023, while PS-InSAR observations begin only in 2016, this makes direct comparison challenging. For 2016, the model likely underestimates deformation because of the lack of real prescribed piezometric head and pumping data. Nevertheless, assuming the modelled trend from 2007 to 2016 continued beyond 2016, metrics were calculated for the overlapping period, including root mean square error (RMSE), R^2, mean absolute error (MAE), mean bias error (MBE), and Pearson correlation coefficient (r). Table 3 summarizes these values for each dataset, indicating varying levels of agreement, with a particularly strong correlation observed between the model and EGMS and TerraSAR-X time series. EGMS achieves an RMSE of only 1.26 mm and a correlation coefficient of 0.987, reflecting near-perfect alignment, while TerraSAR-X shows similarly robust agreement (RMSE = 1.29 mm, $r = 0.921$). Sentinel data processed by StaMPS show the poorest agreement, consistent with its known underestimation of magnitude in this area.

Validation of PS-InSAR results

Validation is conducted only during the time span of Sentinel and TerraSAR-X data because of the absence of GNSS measurements during the ERS and Envisat data, which cover earlier periods (1992–2010). However, this limitation does not undermine the strength of this study's conclusions, as the validated datasets in the more recent years consistently capture the relevant deformation trends, which are key for comparison with the deformation calculated in the geomechanical model.

To validate the PS-InSAR deformation estimations presented in this study, the estimations were compared

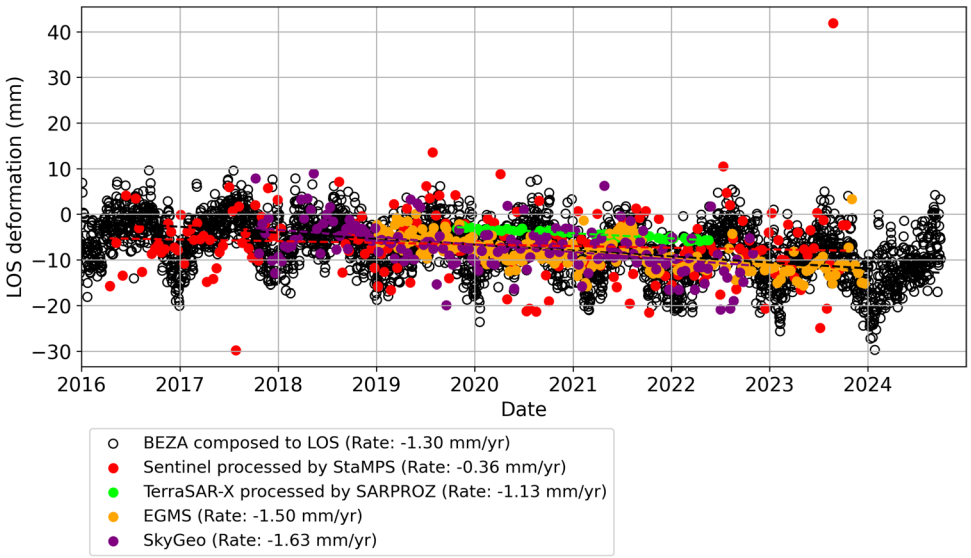

Fig. 12 Comparison between PS-InSAR-derived LOS deformation and GNSS-composed line of sight (LOS) displacement at the BEZA station

with independent data from GNSS station BEZA, located approximately 9.8 km from the centre of the local model area. Although BEZA is not situated directly within the model boundary, it lies within the same radar frame and is processed using the same PS-InSAR dataset. Therefore, any residual atmospheric or processing noise affecting the local model is expected to be similarly present at BEZA.

The GNSS displacement data were taken from BEZA into the LOS direction using satellite acquisition geometry, after which it was compared to four recent independent LOS time series derived from InSAR: Sentinel-1 data processed using StaMPS, TerraSAR-X processed using SARPROZ, Sentinel-1 from the EGMS, and Sentinel-1 from SkyGeo. All PS-InSAR time series were extracted near BEZA to allow direct comparison (Figs. 12). The computed linear trends of LOS deformation rates over the common period are as follows: BEZA GNSS shows –1.30 mm/year, Sentinel processed in StaMPS –0.36 mm/year, TerraSAR-X processed in SARPROZ –2.26 mm/year, EGMS –1.50 mm/year, and SkyGeo –1.63 mm/year. Despite some differences in magnitude, particularly the underestimation by StaMPS, the agreement between BEZA, EGMS, SkyGeo, and TerraSAR-X datasets strongly supports the reliability of the PS-InSAR estimations. This comparison confirms that the observed deformation patterns in this study reflect actual ground motion trends, reinforcing the validity of the PS-InSAR-derived results used throughout the study.

Sensitivity analysis of the 1D geomechanical model

To evaluate the sensitivity of the 1D geomechanical model to changes in specific storage parameters, ten different scenarios were considered with an increase of 100% for the inelastic specific storage in ML 1 and the elastic specific storage in the rest of the MLs. Computed deformations from the 1D geomechanical model under these different scenarios compared to the reference scenario are shown in Fig. 13. Scenario 10 represents the combined effect of a 100% increase in specific storage across all model layers, providing the overall system sensitivity. The sensitivity analysis indicates that a 100% increase in the specific storage of each layer results in varying impacts on computed deformations.

For instance, the cumulative deformation at the end of the period for scenario 5 is –17.6 mm, compared to –13.6 mm in the reference scenario. Results show that ML 4 is the most sensitive layer to changes in specific storage values, where a 100% change in the parameter results in a 27% change in cumulative deformation. For scenario 1 (inelastic specific storage increased by 100% in ML 1), an additional deformation mean rate of 0.44 mm/year during 2009–2016 is computed with respect to the reference scenario. In the case of ML 8, where hydraulic heads are rising, a 100% increase in elastic specific storage results in a 23% decrease in cumulative deformation compared to the reference scenario. This represents the highest swelling from the reference scenario.

On the other hand, MLs 2, 7, and 9 showed the least sensitivity, with an identical cumulative deformation as with the reference scenario. This is because there is nearly no pressure change over the simulated period in these layers, meaning their exact values are less critical and can vary without greatly affecting the model results.

For scenario 10, with a 100% increase in specific storage across all layers simultaneously, the cumulative deformation was significantly different from the reference scenario, indicating the cumulative impact of changes in each layer's specific storage on the total deformation. If the parameters were chosen incorrectly, even a 100% increase in specific storage

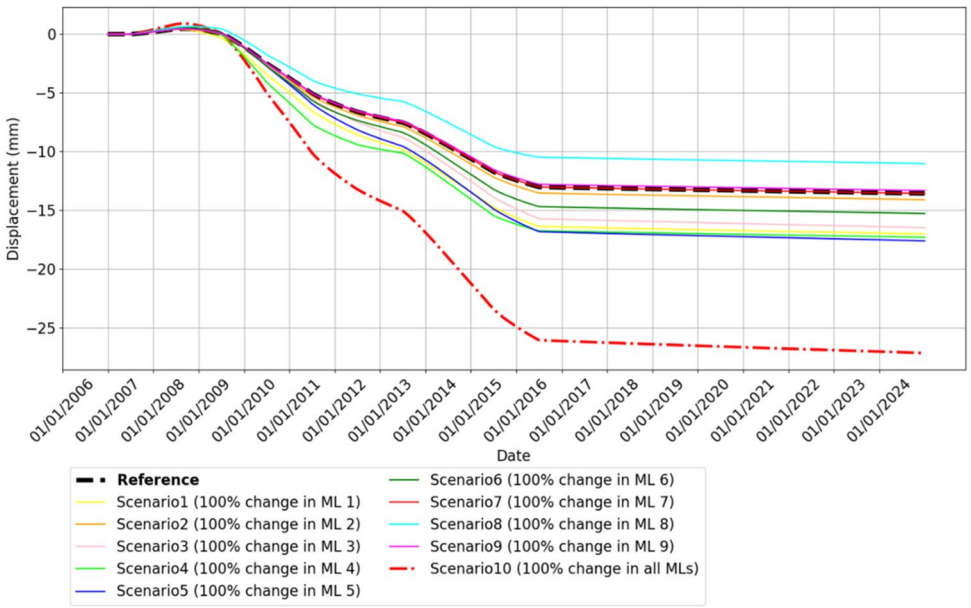

Fig. 13 Comparison of deformations from the 1D geomechanical model under different scenarios, showing the sensitivity to a 100% increase of the inelastic (scenario 1) and elastic (scenarios 2–9) specific storage parameters, and the combined effect (scenario 10)

(which is a modest change in geotechnical terms) would result in a 100% increase in deformation. This highlights the importance of carefully selecting the parameters, as even modest changes can significantly impact the model results.

Discussion

General discussion

In previous studies, it was concluded that the deformation observed by InSAR in the Antwerp region was significant where backfill is present, mainly within the harbour, and that areas without backfill did not experience substantial deformation. Therefore, subsidence was attributed solely to backfill compaction. This interpretation, however, oversimplified the causes of subsidence in the region. By focusing only on backfill compaction, previous studies neglected other potential factors contributing to the deformation. In this study, it was demonstrated that outside of the backfill areas, groundwater abstraction plays a role in subsidence. This study also shows the value of a comparison of PS-InSAR estimation projected onto the vertical direction, with vertical deformation calculated by a sequentially coupled hydro-geomechanical model.

This is illustrated in a case study near Antwerp. A detailed 3D groundwater flow model was developed using MODFLOW, and a customized code was used to execute a 1D geomechanical model based on the same geomechanical equations as the SUB package of MODFLOW (Hoffmann et al. 2003). By dividing the nine MLs into 32 SLs, delay effects for the water pressure propagation in the low-permeability layers was able to be considered. For the study case, the significant hydraulic head declines in the Ruisbroek-Berg Aquifer (ML 4) and the Lower Oligocene Aquifer System (ML 6), lead to notable compaction, whereas the increase in hydraulic head in the Wemmel-Lede Aquifer (ML 8) results in swelling. This swelling compensates for a part of the total compaction, leading to less resulting land subsidence. Additionally, relatively stable hydraulic heads over time in aquitards resulted in minimal deformation, except in ML 5 (Tongeren Aquitard) and its SLs, influenced by the declining hydraulic heads in ML 4 and ML 6. In the polder deposits (ML 1) and Pleistocene and Pliocene Aquifer System (ML 2), the hydraulic heads are only slightly decreasing; however, because of the inelastic deformation in ML 1, slight deformations are computed. No deformation is computed in ML 2, despite experiencing the same negligible hydraulic head decline. The period 2007–2009 was not considered in calculating the rate because of the model dependency on initial conditions, resulting in a slight uplift and unreliable results. During 2009–2016, the maximum deformation was simulated, primarily because this period had the most significant changes in hydraulic heads. After 2016, because of the lack of measured piezometric data, the model output relied only on pumping data from a single well. This is probably quite incomplete, as it may not account for all groundwater abstraction activities of unauthorized pumping in the area, resulting in underestimating deformation after 2016.

This study aligned PS-InSAR datasets (ERS, Envisat, TerraSAR-X, and Sentinel) for visualization purposes. LOS deformation estimations from PS-InSAR were projected in a vertical direction. The ERS data from 1992–2000 indicated

a subsidence trend of –1.9 mm/year, though it did not overlap with the post-2007 deformation phase simulated in the geomechanical model. The Envisat data from 2003 to 2010 showed a rate of –0.3 mm/year within the noise level, with only 3 years overlapping with the model time series. The early stage of the model (2007–2009) can be considered unreliable because of the influence of initial values, and the lack of PS-InSAR data from 2010 to 2016 further complicated comparisons. Post-2016, both the model and PS-InSAR data provided time series, but model results were based on incomplete pumping data. The 1D geomechanical model rate of –1.78 mm/year during 2009–2016 closely matches the SkyGeo, EGMS, and TerraSAR-X rates of –2.67, –2.78, and –2.43 mm/year, respectively.

Considering that in PS-InSAR, detecting small-scale deformations in the millimeter range is challenging because of several inherent limitations, the deformation rates obtained from the different PS-InSAR datasets of SkyGeo, EGMS, and this study's Sentinel processing (all Sentinel based), along with the results of TerraSAR-X, are remarkably consistent. This consistency is a significant achievement, considering the various uncertainties and limitations in the PS-InSAR process, especially the challenge of selecting a stable reference point, which can introduce biases if the reference itself is subject to any movement. On the other side, the 1D geomechanical model sequentially coupled to the 3D hydrogeological model also carries its own set of uncertainties. The model is sensitive to key geomechanical parameters and the accuracy of these parameters directly impacts the deformation simulations. Despite these uncertainties, the model produced a deformation rate of –1.78 mm/year for the 2009–2016 period, which is closely aligned with the deformation rates from the PS-InSAR datasets. This convergence between the model simulation and the PS-InSAR estimations demonstrates a high level of agreement between independent approaches, suggesting that both the model and the satellite-based observations have captured the main mechanisms driving subsidence in the Antwerp local model.

This emphasizes the model's effectiveness in capturing subsidence mechanisms, though comprehensive data integration is crucial for reliable subsidence assessment. The pore pressure profiles have indicated hydrostatic pressure evolution with depth and time, influencing subsidence, and highlighting differences in response between aquifers and aquitards. The sensitivity analysis has shown that changes in specific storage parameters can significantly impact the model results, particularly for some layers such as layers 4 and 5. Despite uncertainties and assumptions in parameter estimation, the combined use of PS-InSAR data and sequentially coupled hydro-geomechanical models provided valuable insights into subsidence mechanisms and driving factors. Future work could specifically focus on obtaining more detailed geomechanical parameters, and also detailed hydrogeological parameters like hydraulic conductivity and specific storage coefficient. However, acquiring more comprehensive and detailed datasets of stress factors, including actual data on groundwater abstraction rates and other transient influences, appears to be crucial. Thus, more extensive and detailed datasets of historical data concerning water pressure changes and pumping changes would significantly enhance the accuracy of subsidence predictions and the overall reliability of the models.

Impact of data scarcity on modelling

The scarcity of piezometric modelledon the border of the local model induced an unknown uncertainty for prescribing boundary conditions that must be acknowledged. A limited number of piezometers were available near the model borders, and all the aquifers considered in the model have not been surveyed. Furthermore, scarce hydrogeological and geomechanical parameter modelledfor several layers compelled the adoption of sample values from nearby regions or from other calibrated models. Another significant issue was the limited amount of modelledabout pumping: until 2016, prescribed piezometric heads could be used; however, thereafter, the model depends solely on a single low-rate pumping well, leading probably to underestimated head declines and deformations post-2016. This constraint reduces the overlap with PS-InSAR observations, which resume in 2016 and extend to 2023. On the other hand, the initial period of the model (2007–2009) was characterized by unstable model conditions resulting from the model starting from an equilibrium state. Therefore, to provide a meaningful comparison, the modelled deformation rate from the robust period (2009–2016) had to be used as a proxy when comparing with PS-InSAR-derived rates post-2016. Despite all these challenges, the close match between the modelled deformation rate over 2009–2016, and the PS-InSAR–derived rates for 2016–2023, provides a validation of the approach used here, while underlining the need for more comprehensive long-term piezometric and pumping monitoring and detailed parameter measurements.

Impact of reference point selection on PS-InSAR estimations

One of the critical factors influencing the accuracy of PS-InSAR measurements is the selection and interpretation of the reference point. In this study, it was assumed that the reference points for all missions (ERS, Envisat, Sentinel, TerraSAR-X, SkyGeo, and EGMS) were stable. Although this assumption is reasonable based on prior knowledge of the physical characteristics of the area, high coherency of the selected point, and geological stability, any slight movement of the reference point could introduce bias into the

displacement calculations. To further mitigate this potential source of error, future research should incorporate the use of geodetic tools such as GPS-equipped corner reflectors, which would provide independent validation of the reference point and enhance the reliability of PS-InSAR estimations.

Conclusions

This study demonstrates that groundwater-induced consolidation contributes to land subsidence in Antwerp. By focusing the modelling on an area beyond the harbour's backfill deposits, thus excluding any backfill-related consolidation, the sole impact of pore-pressure changes on surface deformation was isolated and quantified. With a sequentially coupled 3D-MODFLOW and 1D geomechanical model, a modelled compaction rate of –1.78 mm/year over 2009–2016, which closely matches PS-InSAR estimates of –2.67 mm/year (SkyGeo), –2.39 mm/year (EGMS), and –2.43 mm/year (TerraSAR-X), was quantified. Validation of PS-InSAR datasets against the GNSS station BEZA confirmed the EGMS product as the best fit. It should be mentioned that there was virtually no direct temporal overlap between the robust model period (2009–2016) and the PS-InSAR observations (2016–2023). Consequently, the model-derived subsidence rate from 2009 to 2016 was compared with the PS-InSAR–derived rates from 2016 to 2023, and a close correspondence was still observed. When the 2009–2016 model rate beyond 2016 was linearly projected, this extrapolated trend aligned with the PS-InSAR subsidence rates, thereby validating the magnitude of the modelled rate itself.

These findings reveal that even in the absence of backfill consolidation, possible regional groundwater withdrawals play a measurable role in subsidence and must be accounted for in urban planning. While facing modelledscarcity, the close match between modelled and PS-InSAR deformation affirms the validity of this study's conclusions. Future work should focus on:

1. Extending piezometric and well-pumping monitoring to longer time series;
2. Obtaining detailed in situ geomechanical tests to refine specific storage and conductivity values;
3. Incorporating seasonal head fluctuations in a fully coupled poro-elastic framework; and
4. Applying this workflow at a regional scale.

These advances will further improve subsidence prediction and support sustainable management of groundwater resources.

Acknowledgments This project is conducted within the framework of the BRAIN BELSPO funded LASUGEO project. We extend our gratitude to the European Space Agency (ESA) for providing the satellite images and to the DOV Databank Ondergrond Vlaanderen for the hydrogeological data. We also thank EGMS and SkyGeo for providing complementary data for comparison with our PS-InSAR data. Special thanks to Professor Bertrand François for reviewing part of the paper, Mrs. Leen De Vos, Mrs. Chandra Algoe, and Mr. Johan Lermytte for consulting about data acquisition. We are also grateful to the German Aerospace Centre (DLR) for providing the free TerraSAR-X data through the scientific proposal. Additionally, we thank SARPROZ for providing the processing tool for TerraSAR-X data.

Authors contributions A.CH. carried out the study under the established PhD research framework, collected data, performed the PS-InSAR analyses for Sentinel-1A and Envisat, developed the 1D geomechanical modelling script, ran the 3D MODFLOW simulations, and wrote the first draft of the manuscript. PH.O. supervized the hydrogeological and geomechanical modelling. PY.D. processed the ERS PS-InSAR data. X.D. provided geological oversight. A.D. served as the principal academic supervisor and rigorously reviewed and revised the manuscript.

Funding This research was funded by the BRAIN-Belspo project called LASUGEO, which focuses on monitoring land subsidence caused by groundwater exploitation through geodetic measurements. All authors worked on this project.

Availability of data and materials The datasets generated and/or analysed during the current study are available from the corresponding author on reasonable request.

Declarations

Conflict of interest On behalf of all authors, the corresponding author states that there is no conflict of interest.

Competing interests The authors declare that they have no competing interests.

Ethics approval and consent to participate Not applicable

Consent for publication Not applicable.

References

Abidin HZ, Andreas H, Gumilar I, Fukuda Y, Pohan YE, Deguchi T (2011) Land subsidence of Jakarta (Indonesia) and its relation with urban development. Nat Hazards J 59(3):1753–1771. https://doi.org/10.1007/s11069-011-9866-9

Allen JJ (1973) The effects of stress history on the resilient response of soils. Army Construction Engineering Research Laboratory, Champaign, IL

Baghbani AN, Choudhury T, Costa S, Reiner J (2022) Application of artificial intelligence in geotechnical engineering: a state-of-the-art review. Earth-Sci Rev J 228:103991. https://doi.org/10.1016/j.earscirev.2022.103991

Bejani MM, Ghatee M (2021) A systematic review on overfitting control in shallow and deep neural networks. Artif Intell Rev J 54(8):6391–6438. https://doi.org/10.1007/s10462-021-09975-1

Berardino P, Fornaro G, Lanari R, Sansosti E (2002) A new algorithm for surface deformation monitoring based on small baseline differential SAR interferograms. IEEE Trans Geosci Remote Sens J 40(11):2375–2383. https://doi.org/10.1109/TGRS.2002.803792

Biot MA (1941) General theory of three-dimensional consolidation. Appl Physics J 12(2):155–164. https://doi.org/10.1063/1.1712886

Brinkgreve RB, Vermeer PA (eds) (1999) Plaxis: finite element code for soil and rock analyses, version 7: [user's guide]. Balkema, Rotterdam, The Netherlands

Burbey TJ (2002) The influence of faults in basin-fill deposits on land subsidence, Las Vegas Valley, Nevada, USA. Hydrogeol J 10(5):525–538. https://doi.org/10.1007/s10040-002-0215-7

BGR (Geosciences and Natural Resources), UNESCO (United Nations Educational, Scientific and Cultural Organization) (2013): International hydrogeological map of Europe 1:1,500,000, 25 sheets and 18 explanatory notes. BGR, Hanover, Germany. https://www.bgr.bund.de/EN/Themen/Wasser/Projekte/laufend/Beratung/Ihme1500/ihme1500_projektbeschr_en.html?nn=1557832. Accessed 26 June 2024

Calderhead AI, Therrien R, Rivera A, Martel R, Garfias J (2011) Simulating pumping-induced regional land subsidence with the use of InSAR and field data in the Toluca Valley, Mexico. Adv Water Resour J 34(1):83–97. https://doi.org/10.1016/j.advwatres.2010.09.017

Chaussard E, Bürgmann R, Shirzaei M, Fielding EJ, Baker B (2014) Predictability of hydraulic head changes and characterization of aquifer-system and fault properties from InSAR-derived ground deformation Abstract Key Points Journal of Geophysical Research: Solid Earth 119(8):6572–6590. https://doi.org/10.1002/2014JB011266

Chen X, Tessari G, Fabris M, Achilli V, Floris M (2021) Comparison between PS and SBAS InSAR techniques in monitoring shallow landslides. In: Casagli N, Tofani V, Sassa K, Bobrowsky PT, Takara K (eds) Understanding and reducing landslide disaster risk. WLF 2020. ICL Contribution to Landslide Disaster Risk Reduction. Springer, Cham, Switzerland, pp 155–161

Chen Y, Luo Y, Feng M (2013) Analysis of a discontinuous Galerkin method for the Biot's consolidation problem. Appl Math Comput J 219(17):9043–9056. https://doi.org/10.1016/j.amc.2013.03.104

Chen Y, Tao Q, Hou A, Ding L, Liu G, Wang K (2020) Accuracy verification and evaluation of Sentinel-1A repeat track differential interferometric synthetic aperture radar in monitoring mining subsidence. Appl Remote Sens J 14(1):014501–014501. https://doi.org/10.1117/1.JRS.14.014501

Choopani A, Declercq PY, Orban P, Devleeschouwer X, Dassargues A (2021) Land subsidence as revealed by PS-InSAR observations in the Antwerp area (Belgium): first steps towards the understanding and modeling. In: IAH2021 48th IAH Congress 'Inspiring Groundwater', Brussels, September 2021. https://doi.org/10.13140/RG.2.2.28064.46088

Choopani A, Dehghani M, Nikoo MR (2019) Determining hydrogeological parameters of an aquifer in Sirjan basin using Envisat ASAR interferometry and groundwater modeling. Remote Sens J 41(2):655–682. https://doi.org/10.1080/01431161.2019.1646938

Dassargues A (1995) On the necessity to consider varying parameters in land subsidence computations. In: Barends FBJ, Brouwer FJJ, Schroder FH (eds) Proceeding of the 5th International Symposium on Land Subsidence, The Hague, The Netherlands, 16–20 October 1995. IAHS, Wallingford, UK, pp 258–269

Dassargues A (1998) Prise en compte des variations de la permeabilite et du coefficient d'emmagasinement specifique dans les simulations hydrogeologiques de la consolidation en milieux argileux satures (Taking the variations of hydraulic conductivity and storage coefficient into account for modeling hydrogeological processes and consolidation in saturated clays). Bull Soc Geol Fr 169(5):665–673

Dassargues A (2018) Hydrogeology: groundwater science and engineering. CRC, Boca Raton, FL

Dassargues A, Schroeder C, Li XL (1993a) Applying the Lagamine model to compute land subsidence in Shanghai. Bulletin of the International Association of Engineering Geology 47:13–26. https://doi.org/10.1007/BF02639591

Dassargues A, Radu JP, Charlier R, Li XL, Li QF (1993b) Computed subsidence of the central area of Shanghai. Bull Eng Geol Environ 47:65–88. https://doi.org/10.1007/BF02639592

Databank Ondergrond Vlaanderen 9(DOV) (2024) Geological 3D model (v3.1). Available from the Databank Ondergrond Vlaanderen (DOV). https://www.dov.vlaanderen.be. Accessed 27 June 2024

Davis EH, Raymond GP (1965) A non-linear theory of consolidation. Géotechn J 15(2):161–173. https://doi.org/10.1680/geot.1965.15.2.161

Declercq PY, Gérard P, Pirard E, Walstra J, Devleeschouwer X (2021) Long-term subsidence monitoring of the alluvial plain of the Scheldt River in Antwerp (Belgium) using radar interferometry. Remote Sens J 13(6):1160–1180. https://doi.org/10.3390/rs13061160

Deng YF, Tang AM, Cui YJ, Nguyen XP, Li XL, Wouters L (2011) Laboratory hydro-mechanical characterization of Boom Clay at Essen and Mol. Phys Chem Earth J 36(17–18):1878–1890. https://doi.org/10.1016/j.pce.2011.10.002

Detournay E, Cheng AHD (1993) Fundamentals of poroelasticity. In: Fairhurst C (ed) Analysis and design methods. Pergamon, Oxford, pp 113–171

Domenico PA, Schwartz FW (1997) Physical and chemical hydrogeology. Wiley, New York

Dong S, Samsonov S, Yin H, Ye S, Cao Y (2014) Time-series analysis of subsidence associated with rapid urbanization in Shanghai, China measured with SBAS InSAR method. Environ Earth Sci J 72(3):677–691. https://doi.org/10.1007/s12665-013-2990-y

Duncan JM, Chang CY (1970) Nonlinear analysis of stress and strain in soils. Soil Mech Found Div J 96(5):1629–1653. https://doi.org/10.1061/JSFEAQ.0001458

Ebrahimy H, Feizizadeh B, Salmani S, Azadi H (2020) A comparative study of land subsidence susceptibility mapping of Tasuj Plain, Iran, using boosted regression tree, random forest and classification and regression tree methods. Environ Earth Sci J 79:1–12. https://doi.org/10.1007/s12665-020-08953-0

Eghrari Z, Delavar MR, Zare M, Beitollahi A, Nazari B (2023) Land subsidence susceptibility mapping using machine learning algorithms. ISPRS Int Arch Photogramm Remote Sens Spat Inf Sci 10:129–136. https://doi.org/10.5194/isprs-annals-X-4-W1-2022-129-2023

Faryabi M (2023) A fuzzy logic approach for land subsidence susceptibility mapping: the use of hydrogeological data. Environ Earth Sci J 82(9):209. https://doi.org/10.1007/s12665-023-10909-z

Ferretti A (2014) Satellite InSAR Data: reservoir monitoring from space (EET 9). Earthdoc, New York

Ferretti A, Prati C, Rocca F (2000) Nonlinear subsidence rate estimation using permanent scatterers in differential SAR interferometry. IEEE Trans Geosci Remote Sens 38(5):2202–2212. https://doi.org/10.1109/36.868878

Ferretti A, Prati C, Rocca F (2001) Permanent scatterers in SAR interferometry. IEEE Trans Geosci Remote Sens J 39(1):8–20. https://doi.org/10.1109/36.898661

Ferretti A, Monti-Guarnieri A, Prati C, Rocca F, Massonet D (2007) InSAR principles: guidelines for SAR interferometry processing and interpretation. ESA, Noordwijk, The Netherlands

Findley WN, Lai JS, Onaran K (2013) Creep and relaxation of nonlinear viscoelastic materials. Dover, New York

Fiorentini N, Maboudi M, Leandri P, Losa M, Gerke M (2020) Surface motion prediction and mapping for road infrastructures management by PS-in SAR measurements and machine learning

algorithms. Remote Sens J 12(23):3976–3976. https://doi.org/10.3390/rs12233976
Forster A (2000) Environmental geology: principles and practice. Q J Eng Geol Hydrogeol 33(4):350–351. https://doi.org/10.1144/qjegh.33.4.350-b
Gabrysch RK, Bonnet CW (1975) Land-surface subsidence in the Houston-Galveston region. Texas Water Development Board, Austin, TX
Galloway DL, Burbey TJ (2011) Review: regional land subsidence accompanying groundwater extraction. Hydrogeol J 1486. https://doi.org/10.1007/s10040-011-0775-5
Galloway D, Riley FS (1999) San Joaquin Valley, California: largest human alteration of the Earth's surface. US Geol Surv Circ 1182:23–34
Galloway DL, Jones DR, Ingebritsen SE (1999) Land subsidence in the United States. US Geol Survey. https://doi.org/10.3133/cir1182
Gambolati G, Freeze RA (1973) Mathematical simulation of the subsidence of Venice, 1. Theory Water Resour Res J 9(3):721–733. https://doi.org/10.1029/WR009i003p00721
Gambolati G, Teatini P (2015) Geomechanics of subsurface water withdrawal and injection. Water Resources Res J 51(6):3922–3955. https://doi.org/10.1002/2014WR016841
Gambolati G, Gatto P, Freeze RA (1974) Predictive simulation of the subsidence of Venice. Science 183(4127):849–851. https://doi.org/10.1126/science.183.4127.849
Gedeon M, Wemaere I, Marivoet J (2007) Regional groundwater model of north-east Belgium. Hydrol J 335(1):133–139. https://doi.org/10.1016/j.jhydrol.2006.11.006
Geertsma J (1973) Land subsidence above compacting oil and gas reservoirs. Petrol Technol J 25(06):734–744. https://doi.org/10.2118/3730-PA
Geotechnics Department in Flanders (1999) Report on the results of the drillings with associated laboratory research carried out in connection with the construction of a buffer dike phase in the Waasland Haven in Beveren. Report numbers GEO-00-103/GEO-73-364B/GEO-83-111. Geotechnics Department, Flanders, Belgium
Ghorbani Z, Khosravi A, Maghsoudi Y, Mojtahedi FF, Javadnia E, Nazari A (2022) Use of InSAR data for measuring land subsidence induced by groundwater withdrawal and climate change in Ardabil Plain, Iran. Sci Rep J 12(1):13998–14020. https://doi.org/10.1038/s41598-022-17438-y
Gualandi A, Liu Z (2021) Variational Bayesian independent component analysis for InSAR displacement time-series with application to central California, USA. Journal of Geophysical Research: Solid Earth. https://doi.org/10.1029/2020JB020845
Guzy A, Malinowska AA (2020) State-of-the-art and recent advancements in the modeling of land subsidence induced by groundwater withdrawal. Water J 12(7):2051–2092. https://doi.org/10.3390/w12072051
Heiken G, Funiciello R, Rita DD (2013) The seven hills of Rome: a geological tour of the eternal city in the seven hills of Rome. Princeton University Press, Princeton, NJ. https://doi.org/10.1515/9781400849376
Helm DC (1976) One-dimensional simulation of aquifer system compaction near Pixley, California. Water Resour Res J 11(3):465–478. https://doi.org/10.1029/WR011i003p00465
Helm DC (1986) COMPAC: a field-tested model to simulate and predict subsidence due to fluid withdrawal. Austral Geomech Comput Newslett 10:18–20
Hoffmann J (2003) The application of satellite radar interferometry to the study of land subsidence over developed aquifer systems. Stanford University, Stanford, CA
Hoffmann J, Galloway DL and Zebker HA (2003) Inverse modeling of interbed storage parameters using land subsidence observations. Antelope Valley, California. Water Resour Res 39(2). https://doi.org/10.1029/2001WR001252
Holzer TL, Bluntzer RL (1984) Land subsidence near oil and gas fields, Houston, Texas. Groundw J 22(4):450–459. https://doi.org/10.1111/j.1745-6584.1984.tb01416.x
Holzer TL, Galloway DL (2005) Impacts of land subsidence caused by withdrawal of underground fluids in the United States. In: J Ehlen, WC Haneberg, RA Larson (eds) Humans as geologic agents. Geological Society of America, Boulder, CO. https://doi.org/10.1130/2005.4016(08)
Hooper A (2008) A multi-temporal InSAR method incorporating both persistent scatterer and small baseline approaches. Geophys Res Lett J 35(16):302–307. https://doi.org/10.1029/2008GL034654
Hooper A, Segall P, Zebker H (2007) Persistent scatterer interferometric synthetic aperture radar for crustal deformation analysis, with application to Volcán Alcedo, Galápagos. Geophys Res: Solid Earth J 112(B7):407–428. https://doi.org/10.1029/2006JB004763
Hubbert MK (1957) Darcy's law and the field equations of the flow of underground fluids. Int Assoc Sci Hydrol Bull 2(1):23–59. https://doi.org/10.1080/02626665709493062
Hu L, Wu H, Wen QB (2013) Electro-osmotic consolidation: laboratory tests and numerical simulation. In: The 18th International Conference on Soil Mechanics and Geotechnical Engineering, Paris, September 2013, pp 231–234
Jaeger JC, Cook NGW, Zimmerman R (2009) Fundamentals of rock mechanics. Wiley, Oxford, UK
Jafari F, Javadi S, Golmohammadi G, Karimi N, Mohammadi K (2016) Numerical simulation of groundwater flow and aquifer-system compaction using simulation and InSAR techniques: Saveh basin, Iran. Environ Earth Sci 75:1–10. https://doi.org/10.1007/s12665-016-5654-x
Jang JSR (1993) ANFIS: adaptive-network-based fuzzy inference system. IEEE Trans Syst Man Cybern J 23(3):665–685. https://doi.org/10.1109/21.256541
Jiang L, Bai L, Zhao Y, Cao G, Wang H, Sun Q (2018) Combining InSAR and hydraulic head measurements to estimate aquifer parameters and storage variations of the confined aquifer system in Cangzhou, North China Plain. Water Resour Res J 54(10):8234–8252. https://doi.org/10.1029/2017WR022126
Jorgensen DG (1980) Relationships between basic soils-engineering equations and basic ground-water flow equations. US Government Printing Office, Washington, DC
Khoshghalb A, Khalili N (2010) A stable meshfree method for fully coupled flow-deformation analysis of saturated porous media. Comput Geotechn 37(6):789–795. https://doi.org/10.1016/j.compgeo.2010.06.005
Kim P, Kim YG, Paek CH, Ma J (2019) Lattice boltzmann method for consolidation analysis of saturated clay. Ocean Eng Sci J 4(3):193–202. https://doi.org/10.1016/j.joes.2019.04.004
Labat S (2011) Overview and analysis of 30 years piezometric observations in North-East Belgium (SCK CEN External Report No. SCK*CEN-ER-163). Belgian Nuclear Research Centre (SCK CEN)
Lambe TW (1951) Soil Testing for Engineers. New York: John Wiley and Sons
Leake SA and Galloway DL (2010) Use of the SUB-WT Package for MODFLOW to simulate aquifer-system compaction in Antelope Valley, California, USA. In Land Subsidence, associated hazards and the role of natural resources development: In Proceedings of the eighth international symposium on land subsidence: Queretaro, Mexico, International Association of Hydraulic Sciences (pp 61–67)
Leake S A, Galloway DL (2007) MODFLOW ground-water model: user guide to the subsidence and aquifer-system compaction package (SUB-WT) for water-table aquifers. In: Techniques and Methods (6-A23). US Geological Survey. https://doi.org/10.3133/tm6A23
Lee S, Hong SM, Jung HS (2018) GIS-based groundwater potential mapping using artificial neural network and support vector machine

models: the case of Boryeong city in Korea. Geocarto Int J 33(8):847–861. https://doi.org/10.1080/10106049.2017.1303091
Lewis RW, Schrefler BA (1987) The finite element method in the deformation and consolidation of porous media, 2nd edn. Wiley, Chichester, UK
Li F, Liu G, Gong H, Chen B, Zhou C (2022) Assessing land subsidence-inducing factors in the Shandong province, China, by using PS-InSAR measurements. Remote Sens J 14(12):2875–2896. https://doi.org/10.3390/rs14122875
Li J, Zhu L, Gong H, Zhou J, Dai Z, Li X, Teatini P (2022) Unraveling elastic and inelastic storage of aquifer systems by integrating fast independent component analysis and a variable pre-consolidation head decomposition method. Hydrol J 606:127420. https://doi.org/10.1016/j.jhydrol.2021.127420
Mahmoudpour M, Khamehchiyan M, Nikudel MR, Ghassemi MR (2016) Numerical simulation and prediction of regional land subsidence caused by groundwater exploitation in the southwest plain of Tehran, Iran. Eng Geol J 201:6–28. https://doi.org/10.1016/j.enggeo.2015.12.004
Massonnet D, Feigl KL (1998) Radar interferometry and its application to changes in the Earth's surface. Rev Geophys 36(4):441–500. https://doi.org/10.1029/97RG03139
Mehrnoor S, Robati M, Kheirkhah Zarkesh MM, Farsad F, Baikpour S (2023) Land subsidence hazard assessment based on novel hybrid approach: BWM, weighted overlay index (WOI), and support vector machine (SVM). Nat Hazards J 115(3):1997–2030. https://doi.org/10.1007/s11069-022-05624-0
Miller M, Shirzaei M (2015) Spatiotemporal characterization of land subsidence and uplift in Phoenix using InSAR time series and wavelet transforms. Geophys Res: Solid Earth J 120(8):5822–5842. https://doi.org/10.1002/2015JB012017
Miller M, Shirzaei M, Argus D (2017) Aquifer mechanical properties and decelerated compaction in Tucson, Arizona. Geophys Res: Solid Earth J 122(10):8402–8416. https://doi.org/10.1002/2017JB014531
Ministerie van de Vlaamse Gemeenschap (2004) Departement Leefmilieu en Infrastructuur, Administratie Milieu-, Natuur-, Land- en Waterbeheer, Afdeling Water Ontwikkelen van regionale modellen ten behoeve van het Vlaams Grondwater Model (VGM) in GMS/MODFLOW (Development of regional models for the Flemish Groundwater Model (VGM) in GMS/MODFLOW). Perceel nr. 3: Brulandkrijtmodel (Plot no. 3: Bruland chalk model. Ministerie van de Vlaamse Gemeenschap, Brussels, Belgium
Mirsalari SE, Fatehi Marji M, Gholamnejad J, Najafi M (2017) A boundary element/finite difference analysis of subsidence phenomenon due to underground structures. Minerva Environ Res 8(2):237–253. https://doi.org/10.22044/jme.2016.759
Mitchell JK, Soga K (2005) Fundamentals of soil behavior, vol 3. Wiley, New York
Motagh M, Djamour Y, Walter TR, Wetzel HU, Zschau J, Arabi S (2007) Land subsidence in Mashhad Valley, northeast Iran: results from InSAR, leveling and GPS. Geophys J 168(2):518–526. https://doi.org/10.1111/j.1365-246X.2006.03246.x
Motagh M, Shamshiri R, Haghshenas Haghighi M, Wetzel HU, Akbari B, Nahavandchi H, Roessner S, Arabi S (2017) Quantifying groundwater exploitation induced subsidence in the Rafsanjan Plain, southeastern Iran, using InSAR time-series and in situ measurements. Eng Geol J 218:134–151. https://doi.org/10.1016/j.enggeo.2017.01.011
Nguyen XP, Cui YJ, Tang AM, Li XL, Wouters L (2014) Physical and microstructural impacts on the hydro-mechanical behavior of Ypresian clays. Appl Clay Sci J 102:172–185. https://doi.org/10.1016/j.clay.2014.09.038
Park I, Choi J, Jin Lee M, Lee S (2012) Application of an adaptive neuro-fuzzy inference system to ground subsidence hazard mapping. Comput Geosci J 48:228–238. https://doi.org/10.1016/j.cageo.2012.01.005
Peng M, Lu Z, Zhao C, Motagh M, Bai L, Conway BD, Chen H (2022) Mapping land subsidence and aquifer system properties of the Willcox Basin, Arizona, from InSAR observations and independent component analysis. Remote Sens Environ J 271:112894–112909. https://doi.org/10.1016/j.rse.2022.112894
Perissin D, Wang Z, Wang T (2011) The SARPROZ InSAR tool for urban subsidence/manmade structure stability monitoring in China, In: Proceedings of the 34th International Symposium on Remote Sensing of the Environment, Sidney, April 2011, 1015 pp
Pham HT, Rühaak W, Schuster V, Sass I (2019) Fully hydro-mechanical coupled plug-in (SUB+) in FEFLOW for analysis of land subsidence due to groundwater extraction. Software Man 9:15–19. https://doi.org/10.1016/j.softx.2018.11.004
Pham HT, Rühaak W, Ngo DH, Nguyen OC, Sass I (2020) Fully coupled analysis of consolidation by prefabricated vertical drains with applications of constant strain rate tests: case studies and an open-source program. Geotext Geomembr J 48(3):380–391. https://doi.org/10.1016/j.geotexmem.2019.12.009
Phien-wej N, Giao PH, Nutalaya P (2006) Land subsidence in Bangkok, Thailand. Eng Geol J 82(4):187–201. https://doi.org/10.1016/j.enggeo.2005.10.004
Poland JF, Davis GH (1969) Land subsidence due to the withdrawal of fluids. Rev Eng Geol J 2(1969):187–270. https://doi.org/10.1130/REG2-p187
Poulos HG, Carter JP, Small JC (2002) Foundations and retaining structures: research and practice. Proceedings of the International Conference on Soil Mechanics and Geotechnical Engineering, vol 4. Balkema, Rotterdam, The Netherlands, pp 2527–2606
Prudic DE (1989) Documentation of a computer program to simulate stream-aquifer relations using a modular, finite-difference, ground-water flow model. Department of the Interior. US Geological Survey, Reston, VA
Ray S (2019) A quick review of machine learning algorithms, In: 2019 International Conference on Machine Learning, Big Data, Cloud and Parallel Computing (COMITCon), pp 35–39. https://doi.org/10.1109/COMITCon.2019.8862451
Radhika BP, Krishnamoorthy A, Rao AU (2020) A review on consolidation theories and its application. Geotech Eng J 14(1):9–15. https://doi.org/10.1080/19386362.2017.1390899
Rajabi A M, Abolghasemi Y, Edalat A (2023) Application of support vector machine in modeling land subsidence in parts of Aliabad plain of Qom, Iran. J Eng Geol J 16(1)
Rafiee M, Ajalloeian R, Dehghani M, Mahmoudpour M (2022) Artificial neural network modeling of the subsidence induced by overexploitation of groundwater in Isfahan-Borkhar Plain, Iran. Bull Eng Geol Environ J 81(5):170. https://doi.org/10.1007/s10064-022-02646-7
Reddish DJ, Whittaker BN (2012) Subsidence: occurrence, prediction, and control. Elsevier, Amsterdam
Roscoe KH, Burland J (1968) On the generalized stress-strain behavior of wet clays. Road Research Laboratory. Cambridge University Press, Cambridge, UK
Sato C, Haga M, Nishino J (2006) Land subsidence and groundwater management in Tokyo. Int Rev Environ Strat J 6(2):403–424
Schanz T, Vermeer PA, Bonnier PG (1999) The hardening soil model: formulation and verification. Beyond 2000 Comput Geotech J 1:281–296
Strozzi T, Wegmuller U (1999) Land subsidence in Mexico City mapped by ERS differential SAR interferometry, In: IEEE 1999 International Geoscience and Remote Sensing Symposium (Cat. no.99CH36293). IGARSS'99 4(4):1940–1942. https://doi.org/10.1109/IGARSS.1999.774993
Schiffman RL, Stein JR (1970) One-dimensional consolidation of layered systems. Soil Mech Found Div J 96(4):1499–1504. https://doi.org/10.1061/JSFEAQ.0001453

Schanz T (1998) Zur modellierung des mechanischen verhaltens von reibungsmaterialien (On modeling the mechanical behavior of friction materials). Habilitationsschrift, Mitteilung 45 des Instituts für Geotechnik, Ruhr-Universität, Bochum, Germany

Schofield A, Wroth P (1968) The critical state soil mechanics. McGraw Hill, London

Seed HB (1965) Settlement analysis: a review of theory and testing procedures. Soil Mech Found Div J 91(2):39–48. https://doi.org/10.1061/JSFEAQ.0000721

Shen SL, Xu YS (2011) Numerical evaluation of land subsidence induced by groundwater pumping in Shanghai. Can Geotech J 48(9):1378–1392. https://doi.org/10.1139/t11-049

Sukirman YB, Lewis RW (1994) Three-dimensional fully coupled flow: consolidation modeling using finite element method. In: SPE Asia Pacific Oil and Gas Conference. https://doi.org/10.2118/28755-MS

Tavakkoli Estahbanati A, Dehghani M (2018) A phase unwrapping approach based on extended Kalman filter for subsidence monitoring using persistent scatterer time series interferometry. IEEE J Sel Top Appl Earth Observ Remote Sens 11(8):2814–2820. https://doi.org/10.1109/JSTARS.2018.2837020

Terzaghi K (1925) Principles of soil mechanics. Eng News-Rec J 95(19):742–746

Terzaghi K (1943) Theoretical soil mechanics. Wiley, Hoboken, NJ. https://doi.org/10.1002/9780470172766

Tien Bui D, Shahabi H, Shirzadi A, Chapi K, Pradhan B, Chen W, Khosravi K, Panahi M, Bin Ahmad B, Saro L (2018) Land subsidence susceptibility mapping in South Korea using machine learning algorithms. Sensors 18(8):2464. https://doi.org/10.3390/s18082464

Tosi L, Teatini P, Carbognin L, Brancolini G (2009) Using high-resolution data to reveal depth-dependent mechanisms that drive land subsidence: the Venice coast, Italy. Tectonophys J 474(1):271–284. https://doi.org/10.1016/j.tecto.2009.02.026

van Thienen-Visser K, Pruiksma JP (2015) Breunese JN (2015) Compaction and subsidence of the Groningen gas field in the Netherlands. Proc Int Assoc Hydrol Sci 372(372):367–373. https://doi.org/10.5194/piahs-372-367-2015

Vandersteen K, Gedeon M, Leterme B (2012) Hydrogeology of North-East Belgium. External report. SCK• CEN-ER-236, SCK•CEN, Belgium

Verbeiren B, Batelaan O, De Smedt F (2006) Ontwikkeling van Regionale Modellen ten behoeve van het Vlaams Grondwater Model (VGM) in GMS/MODFLOW. Perceel 1: Centraal Kempisch Systeem. Deelrapport 2: Opbouw van het grondwatermodel, gevoeligheidsanalyse en kalibratie (Development of regional models for the Flemish groundwater model (VGM) in GMS/MODFLOW. Work package 1: Central Campine system. Sub-report 2: Groundwater model construction, sensitivity analysis, and calibration). Vakgroep Hydrologie en Waterbouwkunde (HYDR) - Vrije Universiteit Brussel, Brussels

Vlaamse Milieumaatschappij (2016) Stroomgebiedbeheerplan voor de Schelde 2016-2021: Grondwatersysteemspecifiek deel Centraal Vlaams Systeem, depotnummer, Aalst D/2016/6871/019 (River Basin Management Plan for the Scheldt 2016–2021: groundwater system–specific section, Central Flemish System, deposit number Aalst D/2016/6871/019). Vlaamse Milieumaatschappij, Brussels

Wang YQ, Wang ZF, Cheng WC (2019) A review on land subsidence caused by groundwater withdrawal in Xi'an, China. Bull Eng Geol Environ 78(4):2851–2863. https://doi.org/10.1007/s10064-018-1278-6

Wen T, Tiewang W, Arabameri A, Asadi Nalivan O, Pal SC, Saha A, Costache R (2022) Land-subsidence susceptibility mapping: assessment of an adaptive neuro-fuzzy inference system–genetic algorithm hybrid model. Geocarto Int 37(26):12194–12218. https://doi.org/10.1080/10106049.2022.2066198

Wood DM (1990) Soil behavior and critical state soil mechanics. Cambridge University Press, Cambridge, UK

Xu H, Chen F, Zhou W (2021) A comparative case study of MTInSAR approaches for deformation monitoring of the cultural landscape of the Shanhaiguan section of the Great Wall. Herit Sci J 9(1):1–15. https://doi.org/10.1186/s40494-021-00543-y

Xu YS, Shen SL, Cai ZY, Zhou GY (2008) The state of land subsidence and prediction approaches due to groundwater withdrawal in China. Nat Hazards J 45(1):123–135. https://doi.org/10.1007/s11069-007-9168-4

Yasuhara K, Yamanouchi T, Ue S (1986) Secondary compression of clay in consolidation and undrained shear tests. In: International Symposium on recent developments in laboratory and field tests and analysis of geotechnical problems, Bangkok, December 1983, pp 361–374

Yang W, Xia X (2013) Prediction of mining subsidence under thin bedrocks and thick unconsolidated layers based on field measurement and artificial neural networks. Comput Geosci 52:199–203. https://doi.org/10.1016/j.cageo.2012.10.017

Yun Z (2002) One-dimensional model for land subsidence and its solution. Eng Geol J 10(4):434–437

Zanchettin D, Bruni S, Raicich F, Lionello P, Adloff F, Androsov A, Artale V, Carminati E, Ferrarin C, Fofonova V, Nicholls RJ, Rubinetti S, Rubino A, Sannino G, Spada G, Thiéblemont R, Tsimplis M, Umgiesser G, Vignudelli S, Wöppelmann G, Zerbini S (2021) Sea-level rise in Venice: historic and future trends. Nat Hazards Earth Syst Sci 21(8):2643–2678

Zhang W, Gu X, Hong L, Han L, Wang L (2023) Comprehensive review of machine learning in geotechnical reliability analysis: algorithms, applications, and further challenges. Appl Soft Comput J 136:110066. https://doi.org/10.1016/j.asoc.2023.110066

Zhao K, Chen S (2011) Study on artificial neural network method for ground subsidence prediction of metal mine. Proc Earth Planet Sci J 2:177–182. https://doi.org/10.1016/j.proeps.2011.09.029

Zhou C, Gong H, Chen B, Li X, Li J, Wang X, Gao M, Si Y, Guo L, Shi M, Duan G (2019) Quantifying the contribution of multiple factors to land subsidence in the Beijing Plain China with machine learning technology. Geomorphol J 335:48–61. https://doi.org/10.1016/j.geomorph.2019.03.017

Zhuang C, Zhou Z, Illman WA (2017) A joint analytic method for estimating aquitard hydraulic parameters. Ground Water J 55(4):565–576. https://doi.org/10.1111/gwat.12494

Zienkiewicz OC, Taylor RL (1989) The finite element method: solid mechanics. Butterworth, London